

1202

DETERMINATION OF AERODYNAMIC CHARACTERISTICS
OF BALLISTIC PROJECTILES AT TRANSONIC SPEEDS

Stephen S. Stahara
Nielsen Engineering & Research, Inc., Mountain View, California

ABSTRACT

14 MAY 81

The development of a predictive method for determining the steady inviscid aerodynamic behavior of ballistic projectiles throughout the transonic range is reported. The development has been directed toward establishing the theoretical capability for predicting the static stability characteristics of both the standard conical boattail projectiles as well as a variety of new nonaxisymmetric boattail shapes under study by the U.S. Army. The theoretical procedure employs the classical transonic equivalence rule together with a new loading calculation method which is based on apparent mass concepts and makes use of the nonlinear equivalence rule flow solutions. Theoretical results for surface pressures, loadings, and static aerodynamic characteristics are presented throughout the transonic range for a variety of projectiles. Comparisons are made both with other theoretical methods as well as with experimental results and verify the accuracy of the procedure. Future extension and application of the overall procedure to missile stability and performance is suggested and discussed.

INTRODUCTION

Current projectiles used by the Army are generally slender, spin-stabilized bodies of revolution. The boattail configuration which has become the standard is a conical shape with a relatively shallow cone angle $\sim(5-10^\circ)$. The primary purpose of any boattail is to increase the projectile range by reducing drag from what it would be without boattailing and with the projectile afterbody a straight cylindrical shape (Fig. 1). While a drag reduction is effectively accomplished, mainly through the reduction in base area, a subsequent detrimental result of such a geometric change is the creation of a negative lift on the boattail. This tends to increase even further the destabilizing pitching moment, which already exists due to positive lift on the nose, and consequently acts to reduce additionally the gyroscopic stability of the projectile. At flight speeds within the transonic range, which usually occur near ballistic trajectory apex, the negative loading on the boattail is strongly augmented due to the appearance and movement of shock waves on the aft portion of the boattail. This results in a rapid peaking at flight Mach numbers just below one in the destabilizing pitching moment as well as a similar behavior in other aerodynamic characteristics. Insofar as the aerodynamic derivatives are concerned, this nonlinear behavior due to shock formation and motion is the dominant fluid dynamic characteristic of ballistic projectile flows in the transonic speed regime.

AD A111772

UNC FILE COPY

82 03 09 070

I-199

MAR 8 1982

A

This document is the property of the Department of Defense and is loaned to your organization. It and its contents are not to be distributed outside your organization.

In this regard, and as noted previously,¹ the relative simplicity of basic projectile shapes - which typically consist of an ogive nose followed by a straight cylindrical section and a conical boattail - is deceptive. This is so because the locations where these sections join normally have discontinuities in surface slope and/or curvature; and it is precisely these discontinuities which induce the shock patterns and subsequent sensitive aerodynamic behavior in the transonic range.

In an effort to reduce the adverse transonic behavior of ballistic projectiles, the Army has recently investigated experimentally² a series of nonaxisymmetric boattail shapes. Some of these nonstandard shapes were found to improve significantly the projectile aerodynamic characteristics over those of the conical configuration. In particular, it was found that both increased gyroscopic and dynamic stability and decreased drag could be attained simultaneously, so that for the first time projectile designs were feasible which not only provide increased range over the standard boattail shapes but also improved stability.

The present work describes the development of a theoretical method for predicting the transonic static aerodynamic characteristics of these projectiles. The objective has been the enablement of a rational modeling of the aerodynamic effects of incorporating different axisymmetric and nonaxisymmetric boattail geometries into ballistic projectile design with a view toward optimizing the aerodynamic performance of these shapes. The theoretical analysis for determining the nonlinear three-dimensional projectile flow fields is based on the classical transonic equivalence rule (TER); and employs finite-difference successive line over-relaxation (SLOR) solutions of the axisymmetric transonic small-disturbance potential equation for the outer nonlinear flow region, and finite-element solutions of the cross flow Laplace equation to determine the nonaxisymmetric inner flow region.

A new loading calculation method which is based on apparent mass concepts and which makes use of nonlinear equivalence rule flow solutions is used to predict the static aerodynamic coefficients. Theoretical results for surface pressures, loadings and static aerodynamic coefficients are presented for a variety of projectiles with different boattail geometries at Mach numbers throughout the transonic range. Comparisons are made insofar as possible with both other theoretical methods and experimental results.

ANALYSIS

GENERAL

The most notable feature of transonic flow past typical ballistic projectiles is the formation and movement as a function of oncoming Mach number of a variety of shock waves both on the surface and in the flow field of these configurations. This is clearly evident in shadowgraphs such as those shown in Figure 2, which illustrate the characteristic shock formation and movement on such shapes as the Mach number increases beyond subcritical.

The result of the rapid formation and movement of shock waves on the aerodynamic characteristics of typical projectiles in the transonic regime is a sharp peaking in their behavior in the vicinity of $M_\infty = 1$. As indicated in the sketches in Figure 3, both the overturning pitching moment coefficient and drag strongly exhibit this behavior. With regard to pitching moment, the sketch in Figure 3 displaying a typical projectile shock pattern illustrates clearly why this occurs. At angle of attack, the shock positions on the windward surface are displaced farther aft than on the leeward side, resulting in a strong negative loading at those axial locations. Both shock strengths and negative loading are strongest by a considerable amount for the boattail shock. As the Mach number increases and the boattail shock moves further aft, both the strength of the negative loading and its moment arm from the center of mass of the projectile increase, and result in a peak pitching moment occurring just prior to the shock moving off the boattail. This inevitably occurs at a Mach number just below one. As the Mach number increases beyond that value, the destabilizing pitching moment decreases rapidly and usually smoothly, and then eventually plateaus as the Mach number increases further supersonically.

BASIC EQUATIONS AND BOUNDARY CONDITIONS

The coordinate system employed in the analysis is a body-fixed Cartesian system with origin at the nose of the configuration, and orientation such that the x axis is directed downstream and coincident with the longitudinal body axis, and the y axis to the right facing forward, and the z axis directed vertically upward, as illustrated in Figure 4. The oncoming free-stream may be inclined in pitch to the x axis at some arbitrary small angle, α , but sideslip has not been considered. The flow is assumed to be inviscid and steady, and the configurations sufficiently slender and smooth that the resulting flow field is irrotational and adequately treated by small-disturbance theory. Accordingly, a disturbance velocity potential ϕ can be defined by:

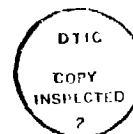
$$\phi(x,y,z) = U_\infty \ell [x + \alpha z + \phi(x,y,z)] \quad (1)$$

where ϕ is the total velocity potential, U_∞ represents the freestream velocity, ℓ is the body length, and the coordinates (x,y,z) have been nondimensionalized by ℓ . The governing partial differential equation for ϕ , appropriate for the low-lift slender configurations considered, is given by:

$$(1-M_\infty^2)\phi_{xx} + \phi_{yy} + \phi_{zz} = \frac{\partial}{\partial x} \left[\frac{1}{2} M_\infty^2 (\gamma+1) \phi_x^2 \right] \quad (2)$$

We note that the quadratic terms $(\phi_x^2 + \phi_z^2)$, which usually appear^{4,5} within the bracket on the right-hand side to account for situations where the lift is significant, are of higher order and negligible for the thickness-dominated situations of interest here. For the body-fixed coordinate system shown in Figure 4, the expression for the pressure coefficient is given by:

$$C_P = \frac{p-p_\infty}{\rho_\infty U_\infty^2 / 2} = -2(\phi_x + \alpha \phi_z) - (\phi_y^2 + \phi_z^2) \quad (3)$$



12th Army Research
and/or
Dist Special
A

In general, the boundary conditions to be satisfied consist of: (1) far-field conditions appropriate to the behavior of the flow far removed from the body in either a free-air flow or in a wind tunnel environment; (2) the body surface condition that the velocity component normal to the body surface be zero at the body; and (3) shock wave conditions to be applied at any shock surface appearing in the flow, such that the potential is continuous through the shock and the velocity components satisfy the small disturbance approximation to the Rankine-Hugoniot conditions at the location of the shock. These requirements lead for slender shapes to the following condition on ϕ for free-air flows:

$$\phi(\alpha) = 0 \quad (4)$$

$$[n_1 + \alpha n_3] + n_2 \phi_y + n_3 \phi_z \Big|_{\text{body}} = [(n_1 + \alpha n_3) + \phi_n]_{\text{body}} = 0 \quad (5)$$

$$[\phi]_{\text{shock}} = 0,$$

$$\left\{ [(1 - M_\infty^2) - M_\infty^2(\gamma + 1) \langle \phi_x \rangle] [\phi_x] + [\phi_y^2] + [\phi_z^2] \right\}_{\text{shock}} = 0 \quad (6)$$

where $n = i n_1 + j n_2 + k n_3$ is the unit normal to the body surface, (n_1, n_2, n_3) are the direction cosines of n with respect to the (x, y, z) axes and the symbols $[\]$ and $\langle \ \rangle$ signify the difference and the mean, respectively, of the enclosed quantity on the two sides of the shock surface.

TRANSONIC EQUIVALENCE RULE FOR THICKNESS DOMINATED FLOWS

The transonic equivalence rule (TER) was developed initially in the form, now known as the classical or thickness-dominated limit, by Oswatitsch^{6,7} for thin nonlifting wings, and extended later to moderately lifting wings⁸ and slender configurations of arbitrary cross section³. Subsequent extensions of the rule^{4,5,9} to include situations where the lift is significant both revealed its dependence on lift as well as clarified the classical limit and range of validity. In essence, the rule provides the basis for greatly simplifying the calculation of transonic flows past a special but aerodynamically important class of three-dimensional configurations. It accomplishes this by recognizing that the structure of transonic flows past slender shapes in the vicinity of $M_\infty \approx 1$ consists of two distinct but coupled domains whose governing equations and boundary conditions are significantly easier to solve than the original equations, Equations (2) and (4)-(6). For flows at low to moderate lift conditions, such as those typical for stable projectile flight, the solution domains consist of an inner region governing by a linear equation, the same as in slender-body theory, and an outer nonlinear region consisting of the axisymmetric flow about an "equivalent" nonlifting body of revolution having the same longitudinal distribution of cross-sectional area.

The theoretical essentials of the equivalence rule for thickness-dominated flows past slender configurations are illustrated in Figure 4, which displays the decomposition of the flow into its first-order inner and outer components, and the resulting uniformly valid composite solution; that is

$$\phi = \phi_{2,\alpha} + \phi_{2,t} + \phi_{2,\omega} - \phi_{2,B} + \phi_B \quad (7)$$

Here each component of ϕ has the meaning indicated in Figure 4. The first-order lift ($\phi_{2,\alpha}$), thickness ($\phi_{2,t}$), and rotation ($\phi_{2,\omega}$) inner solutions describe, respectively, the translating, expanding and rotating cross section in the y,z plane, and satisfy the two-dimensional Laplace equation

$$\phi_{2yy} + \phi_{2zz} = 0 \quad (8)$$

together with the no-flow boundary condition in the y,z plane at the body surface at each x station. The first-order outer solution, ϕ_B , satisfies the axisymmetric transonic small-disturbance equation:

$$(1 - M_\infty^2)(\phi_B)_{xx} + (\phi_B)_{rr} + (1/r)(\phi_B)_r = [M_\infty^2(\gamma + 1)(\phi_{Bx})^2/2]_x \quad (9)$$

subject to an inner boundary condition determined by the "equivalent" body singularity source distribution. This, in turn, is determined by the outer behavior ($\phi_{2,B}$) of the inner solution:

$$\lim_{r \rightarrow 0} [r(\phi_B)_r] = \lim_{r \rightarrow 0} r[\phi_{2,\alpha} + \phi_{2,t} + \phi_{2,\omega}] = r(\phi_{2,B})_r = S'(x)/2\pi \quad (10)$$

where $S(x)$ is the equivalent body cross-sectional area nondimensionalized by ξ^2 , and the effects of lift and rotation are recognized to be small in comparison to thickness effects, so that their contribution to the outer flow is of a higher order. Shock conditions appropriate to the outer flow are given by:

$$\begin{aligned} & \llbracket \phi_B \rrbracket_{\text{shock}} = 0, \\ & \left\{ r[1 - M_\infty^2 - M_\infty^2(\gamma + 1)\phi_{Bx}] \llbracket \phi_{Bx}^2 \rrbracket + \llbracket (r\phi_{Br})^2 \rrbracket \right\}_{\text{shock}} = 0 \end{aligned} \quad (11)$$

The final boundary condition for the outer problem relates to conditions representative of the flow far from the configuration. For free-air flows at infinity this is given by Equation (4). Appropriate asymptotic conditions for a bounded free-air domain or a tunnel environment are discussed in the following section.

Higher order TER solutions for thickness-dominated flows beyond the first-order terms indicated in Equations (7)-(11) can be determined systematically by the methods described in References 4 and 5. These consist of a doubly infinite coupled series of inner and outer solutions. In general, the higher order inner solutions satisfy a Poisson equation in the crossflow plane, with the right-hand side a known function of lower order inner solutions and satisfy a linear equation with nonconstant coefficients dependent on the first-order outer (ϕ_B) solution. For the results presented here, only the first-order components are employed.

OUTER FLOW SOLUTION

The method employed to determine the outer flow component, ϕ_B , satisfying Equations (9)-(11) is a finite-difference SLOR procedure using Murman-Cole type-dependent difference operators¹⁰⁻¹². To realize the calculation, we have

employed the following fully conservative form of Equation (9):

$$[\eta(K\bar{\zeta}_x - \bar{\zeta}_x/2)]_x + [\eta\bar{\zeta}_\eta]_\eta = 0 \quad (12)$$

where

$$\bar{\zeta}(x, \eta) = (1/\tau^2)\zeta_B(x, r), \quad K = (1 - M_\infty^2)/(\tau^2 M_\infty^2)(\gamma + 1), \quad \eta = \tau M_\infty \sqrt{\gamma + 1} \tau \quad (13)$$

and τ signifies the thickness ratio of the equivalent body. The finite-difference form of the equation actually solved is that suggested by Jameson¹³ in terms of a correction potential. Additionally, a pseudotime term of the form $-(\Delta t/\Delta x)\phi_{Bxt}$ was added to enhance stability and speed convergence. The inner boundary condition, Equation (10), becomes

$$\lim_{\eta \rightarrow 0} (\eta \bar{\zeta}_\eta) = \frac{\bar{S}(x)}{2\pi} \quad (14)$$

where $\bar{S}(x) = S(x)/\tau^2$.

For free-air flows, since the boundaries of the computational mesh employed are at a finite rather than infinite distance from the origin, a more accurate representation of the far-field potential which reflects its asymptotic behavior should be employed rather than Equation (4). These conditions depend, of course, upon the free-stream Mach number and are different for subsonic, sonic, and supersonic oncoming conditions. The appropriate boundary conditions employed on the computational domain at the upstream, lateral, and downstream boundaries are given in detail in Reference 14 and are summarized in Figure 5, where both the inner and outer conditions are provided.

Verification of the accuracy and versatility of the outer flow solution procedure has been made by extensive comparisons with data. These results are reported in Reference 14 and cover a variety of different body shapes at Mach numbers throughout and beyond the transonic range. The corresponding comparisons with data taken in conventional ventilated transonic tunnels indicated excellent agreement.

INNER FLOW SOLUTION

The determination of the inner flow problem consists of solving the crossflow Laplace Equation (8) for the three first-order inner components, $\phi_{2,\alpha}$, $\phi_{2,t}$ and $\phi_{2,\omega}$, corresponding to the vertical translation, expansion, and rotation, respectively, of the projectile cross section in the y, z plane. The component $\phi_{2,B}$ in Equation (7) represents the outer behavior of the inner solution, and for the thickness-dominated flows considered here is given analytically by [see Eq. (10)]

$$\phi_{2,B} = \frac{S'(x)}{2\pi} \ln r \quad (15)$$

For the axisymmetric portion of the projectile, the three inner solutions can be determined analytically, and are

$$\psi_{2,a} = \frac{\alpha S(x)}{r} \cdot \frac{\sin \alpha}{r} \quad (16)$$

$$\psi_{2,t} = \frac{S'(x)}{2r} \ln r \quad (17)$$

$$\psi_{2,w} = 0 \quad (18)$$

Along the nonaxisymmetric boattail, general analytic expressions cannot be given for typical cross-sectional shapes of interest to this study. Those shapes comprise a general class of contour: formed by $N(N \geq 3)$ equal-length, flat-sided segments separated by N equal-angle circular arc segments, and are formed by cutting planes acting on the axisymmetric projectile boattail. Those cutting planes are inclined at a small angle to the main projectile axis, and result in flat surfaces being formed longitudinally on the boattail. In general, these cutting planes may also rotate about the projectile axis as they proceed downstream so as to provide twist to the cut surface and thereby prevent projectile despinning. Figure 6 provides an illustration of two such boattail shapes formed by employing three and four cutting planes. For these shapes, the basic axisymmetric boattail was cylindrical rather than conical, the cutting planes were not rotated, and the cutting plane angles and axial starting locations were chosen such that the cutting planes meet at the boattail end and result in an inscribed triangle and square, respectively.

The computational method employed to determine the inner flow solutions is a finite-element procedure. The procedure uses the Galerkin method of weighted residuals and employs isoparametric quadrilateral elements with quadratic shape functions of the serendipity type. The linear, symmetric matrix equations that result from discretization of the Laplace equation are solved directly using Gaussian elimination. The body surface boundary conditions for each of the three inner computational problems are summarized in Figure 7. In the computational procedure they are implemented via a Neumann (flux) condition. On the outer boundary of the finite element mesh, Neumann conditions are also employed for each of the component problems, as this was found to be much more convenient and of essentially equal accuracy as the corresponding Dirichlet conditions. A typical finite element mesh employed for these calculations is illustrated in Figure 8. That figure displays the mesh for a body formed by three cutting planes acting on a circular cross section such that a sectored triangular shape results in which the circular arc segments subtend 30° angles. The mesh shown consists of six rings extending radially outward from the body surface and having 12 quadrilateral elements per ring. The radial spacing of the rings is geometrical, and for the mesh illustrated here the spacing ratio was 1.4.

A series of numerical experiments were performed in order to examine inner solution accuracy as a function of mesh parameters, viz. number of rings, number of elements per ring, radial mesh spacing ratio, and outer boundary location. The results indicated that mesh configurations similar to that shown in Figure 8 were adequate with regard to both number of rings and elements per ring, provided that the outer boundary was located at approximately 8 body radii and that radial mesh spacing near the body surface

was slightly more compact than that shown in the figure. A geometric ratio of 2.0 was found to be satisfactory.

Figure 9 provides an indication of the typical accuracy of the finite-element solver when applied to one of the three component inner problems. Displayed are the surface velocity components for the contraction problem for the 30° sector triangular cross section shown previously in Figure 8. The predicted velocities shown are adjusted to be relative to the local body surface, and thus should be entirely tangential to the local surface. The particular contraction problem solved here was for a unit contraction of the flat segments ($\phi_n = dF/dx = -1$) and with the circular arc segments stationary ($\phi_n = dR/dx = 0$). The surface velocity vectors are shown at the surface node point locations. As can be seen, the velocity vectors on both the flat and circular segments are indeed essentially tangential to the local surface. At the junctions of the flat and circular segments, two vectors are indicated since for those points a velocity vector can be predicted employing values of the potential associated either with the element lying on the circular segment or the adjacent element lying on the flat segment. Potential theory is in fact discontinuous at those locations; and although velocities exactly at those corner points are never used or required in any of the calculations performed here, it is nevertheless instructive to observe the behavior of the finite-element solver at those singular points. As is evident from the results shown in Figure 9, the solver provides both the correct trend (high magnitude) and direction (tangential to the surface) of the solution behavior at those locations. From additional numerical experiments involving both an examination of surface pressures in the vicinity of these points, as well as contour integrals of surface velocity and potential about the entire cross section (in order to determine apparent mass coefficients, see section following, we have verified that the finite-element solver is capable of adequately resolving the flow behavior in the vicinity of the corners and providing rapid and accurate solutions for all the inner problems for the geometries of interest here.

LOADING CALCULATIONS

The objective of the development and application of the TER procedure to ballistic projectiles was to provide the means for determining the 3-D transonic flow fields about these shapes and, subsequently, the surface pressures and the resultant steady aerodynamic forces and moments. Since the primary utility of the present predictive method to projectile applications, however, is in the accurate determination of those static aerodynamic characteristics, the calculation and subsequent integration of surface pressures predicted via the TER method over the entire projectile is an undesirable intermediate, computationally-expensive step. Consistent with the order of accuracy of the present flow solution, it is possible to formulate a procedure based on the TER solution and slender body theory which avoids that step and provides the axial loading distribution directly.

This procedure, known as the method of apparent masses¹⁵, relates the kinetic energy of the fluid per unit axial length to contour integrals involving various crossflow velocity potentials describing the translation, rotation, etc., of the cross section and their normal gradients on the local surface. These contour integrals are relatable to the apparent mass coeffi-

icients of the configuration cross section; and with those coefficients in hand, the determination of the lateral force and moment distributions is direct.

The utility of the apparent mass method is in the determination of stability derivatives, both static and dynamic, for slender configurations. The method has been successfully employed in the past in a wide number of aerodynamic applications¹⁶, particularly for missile configurations. A detailed formulation of the method for combined upwash, side-wash, and roll including derivations of all the important static and dynamic stability derivatives is provided in Reference 19. Such previous applications of the method have focused exclusively in the subsonic and supersonic regimes where the governing small-disturbance potential equations are linear. Since slender body theory is equally valid throughout the transonic regime as well, and in fact underlies the basis of TER method, application of the apparent mass method at transonic speeds is certainly feasible. However, a well-known result of the classical TER method³⁻³, and actually verified by experiment for certain classes of aerodynamic configurations³, is that the loading distributions and hence the lateral forces and moments are independent of oncoming Mach number. This, of course, is not the case for typical projectiles, as noted in Figure 3. The reason for this discrepancy lies not in an overall breakdown of the TER procedure, but rather in the failure to take into account locally the large axial gradients which occur in the vicinity of shock waves located on the body surface. These large gradients locally violate the moderate axial gradient hypothesis inherent in the apparent mass method.

Because of the deficiency of the procedure for applications at transonic speeds is associated primarily with the behavior of the axial velocity component in the vicinity of shock waves, we have postulated and successfully tested the following modification of the classical apparent mass method: (1) correct the axial velocity in the classical apparent mass formulation by replacing the free-stream velocity by the local axial velocity, and (2) apply a similar correction to the lateral velocities. Here, the axial perturbation velocity component to be added locally to the free-stream velocity can be considered as provided by the TER composite solution Equation (7). However, since the effect we are attempting to correct for is a transonic one due to nonlinear Mach number dependent variations in the vicinity of shock waves, and since the two-dimensional crossflow solutions contained in Equation (7) are independent of M_∞ , it is sufficient to consider the local axial velocity as augmented by the equivalent body perturbation axial velocity alone, viz.

$$V_x \approx 1 + \phi_{B_x} \quad (19)$$

In order to implement these ideas, consider the normal force loading distribution dC_N/dx for combined angle of attack, α , sideslip, β , and roll rate, p , of a typical ballistic projectile. (Although we have not considered sideslip in our derivations of the TER method, it would be a straightforward extension to do so.) The transonically corrected classical loading distribution¹⁶ is given by:

$$\frac{dC_N}{dx} = 2 \left\{ V_x \frac{\partial}{\partial x} [M_{12}v_1 + M_{22}v_2 + M_{23}p] - p[M_{11}v_1 + M_{12}v_2 + M_{13}p] \right\} \quad (20)$$

where

$$M_{ij} = - \oint_C \zeta_i \frac{\partial \zeta_j}{\partial n} \quad (21)$$

$$V_x = 1 + \zeta_{B_x} \quad (22)$$

$$v_1 = f(1 + \zeta_{B_x}) \quad (23)$$

$$v_2 = a(1 + \zeta_{B_x}) \quad (24)$$

Here, the M_{ij} are apparent mass coefficients determined from the following inner flow solution representation (see Fig. 4)

$$\zeta_2 = f\zeta_1' + a\zeta_2' + p\zeta_3' + \zeta_{2,t} \quad (25)$$

where ζ_1', ζ_2' represent crossflow potentials for unit horizontal and vertical translation, respectively, of the cross section, ζ_3' represents the potential for unit angular velocity of the cross section about the longitudinal axis, v_1, v_2 are the transversally corrected sidewash and upwash, and the normal force coefficient is defined by

$$C_N = Z / \frac{1}{2} \rho_\infty V_\infty^2 \pi R_{\max}^2 \quad (26)$$

Thus, for a projectile having a conical boattail for which the apparent mass coefficients are known analytically ($M_{11} = M_{22} = \pi R^2$, $M_{12} = M_{23} = M_{13} = 0$), at zero sidewash ($f = 0$) and roll rate ($p = 0$), the normal force loading distribution is given by

$$\frac{dC_N}{dx} = 2a(1 + \zeta_{B_x}) \cdot \frac{d}{dx} \left[(1 + \zeta_{B_x}) \cdot \left(\frac{R}{R_{\max}} \right)^2 \right] \quad (27)$$

Corresponding results for the static normal force and overturning pitching moment coefficients $C_{N_\alpha}, C_{m_\alpha}$ are found from

$$C_{N_\alpha} = \frac{\partial}{\partial \alpha} \int_0^1 \frac{dC_N}{dx} dx \quad (28)$$

$$C_{m_\alpha} = \frac{\partial}{\partial \alpha} \int_0^1 (x_{c_m} - x) \frac{dC_N}{dx} dx \quad (29)$$

where x_{cm} is the overturning moment center and the pitching moment is defined as positive nose-up.

In general, for the nonaxisymmetric cross sections such as those of interest here, the apparent mass coefficients cannot be determined analytically and must be found numerically. The finite-element solver described in the previous section provides a convenient means of readily determining these coefficients. Consequently, although both inner and outer TER solution procedures are necessary to determine the projectile loading distribution, viz. the finite-element inner solver to calculate the apparent mass coefficients of the projectile cross section, and the SLOR solver to calculate the axisymmetric nonlinear transonic flows past the equivalent body of revolution, the determination of the detailed surface pressures and their integration over the body surface is avoided.

In order to test the loading procedure, we have applied the method to a variety of different projectiles having both axisymmetric and nonaxisymmetric boattail geometries at Mach numbers throughout the transonic range. In the following section, we provide some typical results of such calculations, together with comparisons with other theoretical methods and data.

RESULTS

To examine the applicability of the transonic equivalence rule for determining transonic flows past ballistic projectiles, as well as to test the validity and accuracy of the proposed nonlinear loading procedure, we have applied these procedures to predict the surface pressures, loading distributions, and static aerodynamic coefficients of a variety of different projectiles at flow conditions throughout the transonic range. In the following sections, we provide some selected results typical of the projectile calculations that were performed. Comparisons with data and as far as possible with other theoretical methods are provided.

SURFACE PRESSURES

Insofar as the basic validity and range of accuracy of the TER method for predicting transonic flow fields past slender bodies are concerned, extensive comparisons of TER results with data have been made and are provided in Reference 17. In that study, experimental results and TER theory were compared for body surface pressures obtained in conventional transonic tunnels for a number of different axisymmetric and nonaxisymmetric shapes. The configurations included both smooth bodies as well as projectile-like discontinuous slope shapes. Those results, which also incorporated wind tunnel interference effects, provide the most extensive comparison of the classical equivalence rule with experiment. They indicate good agreement with data, including the region near shock waves, at oncoming Mach numbers throughout and beyond the transonic regime for low to moderate angles of attack.

Here, we provide some further results for specific projectile shapes. In Figure 10 we have exhibited TER results for the surface pressure coefficient on a secant ogive nose, straight cylindrical midbody, and 7° conical

boattail projectile at $M_\infty = 0.94$ and $\alpha = 4^\circ$. These results display typical axial and azimuthal surface pressure variations characteristic of transonic flows past standard ballistic projectile shapes. The most notable feature of the results in Figure 10 is the prominent expansion and compression spikes in the vicinity of the nose/midbody and midbody/boattail junctures; and are associated with the acceleration and deceleration of the flow in those regions where the surface geometry is discontinuous.

The TER results display the surface pressure along longitudinal rays at the windward, leeward, and midbody azimuthal positions. For this axisymmetric boattail projectile shape, the inner flow solutions are provided analytically everywhere by Equations (16)-(18). The outer flow equivalent body finite-difference solution used in these results employed an (x,r) mesh density of 140x40 points with 100 equally spaced points on the body. The r grid as well as the x grid ahead and behind the body were expanded using a grid ratio of 1.2:1. The x mesh extended 2 body lengths ahead of the nose and 2 body lengths behind the tail of the body, and the location of the first radial grid line was at $r = 1/2$. The r mesh extended laterally to 5 body lengths. This grid was the standard one employed in determining all of the equivalent body solutions reported here.

Also shown in Figure 10 are Reklis's¹⁸ three-dimensional transonic small-disturbance results for pressures along the windward ray. The agreement between the two theoretical methods is quite good everywhere, with the only exception being some minor disagreement in the pressure spike regions near the nose/midbody and midbody/boattail junctures. At those locations, the TER results predict a slightly higher and earlier expansion. However, it is probable that even these slight discrepancies are attributable to different grid densities and/or boundary condition treatment in those locations rather than from the difference in the level-of-approximation of the two methods.

LOADING DISTRIBUTIONS

In order to check and verify the proposed loading calculation method for applications to ballistic projectiles, we have employed it to predict loadings on a number of different projectile shapes for which results from other theoretical methods are available. Figure 11 presents a comparison of results for the normal force distribution on an idealized 5.6 caliber length M549 projectile at $M_\infty = 0.95$ and $\alpha = 1^\circ$. For these comparisons, the geometry of the actual projectile shape has been simplified by considering the nose as sharp, by neglecting the rotating bands, and by simulating the afterbody wake geometry by extending the conical boattail beyond the actual projectile length.

In addition to the present method, results from the three-dimensional transonic small-disturbance (3-D TSD) procedure of Reklis¹, from three-dimensional Euler equations calculations¹⁹, and from slender body theory are provided in the figure. On the ogive nose, the present method and the Euler equation result compare quite closely, and are only moderately removed from the slender body result. However, the 3-D TSD results predict a noticeably higher loading. On the cylindrical midbody, the present method indicates a slight positive loading at points beyond the immediate vicinity of the ogive/midbody juncture; whereas, the Euler results predict a negative

loading over the majority of the cylindrical midbody, and the 3-D TSD results show essentially no loading at all. The slender body loading along that unchanging cylindrical cross section is, of course, zero.

As the discontinuity in surface slope at the midbody/boattail juncture is approached and passed, the present method displays first a large positive then negative loading spike corresponding to the rapid flow expansion and compression at the location. Downstream of that juncture, the present theory displays another sharp spike, due to the boattail shock. Once beyond the boattail shock, the present method essentially provides the slender body result. Along the boattail, the corresponding 3-D TSD result displays no expansion spikes at the boattail juncture. However, similar to the present theory, that result does indicate the same strong downward loading spike on the main boattail section due to the boattail shock, although that peak is displaced slightly rearward from the present theory prediction. With regard to the Euler equation prediction on the boattail, a positive loading is indicated just beyond the boattail juncture and then an increasing negative loading on the remainder of the boattail. In the calculation, the boattail was extended to $x/D = 6.5$ at which point for numerical convenience a spherical cap was added to close the body. That spherical cap, which was located sufficiently far downstream so as not to influence the solution on the actual projectile, locally induces a sharp discontinuous behavior which is to be disregarded. At first glance, the Euler result appears to be quite different from the present theory and the 3-D TSD result over the major portion of the boattail. That is in fact not the case since the Euler prediction was carried out on a much coarser computational grid than both the present method and the 3-D TSD calculation. That has resulted in a broad smearing of the boattail shock, and it is felt that increasing the grid density would result in good correspondence between the Euler result and the present method. In particular, we observe that as in the present result, a positive expansion loading exists in the Euler prediction near the boattail juncture. Finally, with regard to the overall agreement evident from this comparison, we note that the present loading method is able to capture all of the critical features of the loading behavior for this typical projectile geometry as predicted by other more accurate but computationally far more expensive procedures.

In Figure 12, we present an additional loading comparison between the present method and Euler equation solutions¹⁹. These are intended to illustrate the loading behavior both as a function of Mach number throughout the transonic range and also for extremes of projectile geometry. That figure provides a comparison of the normal force distribution on a slender 12 caliber length projectile having a 5 caliber cylinder midbody, and 2 caliber 10° conical boattail. For the Euler calculations, a small spherical cap was added at the base of the projectile, while for the present method, the conical base was extended downstream. Results are displayed for $M_\infty = 0.75, 0.90, 0.95$ at $\alpha = 1^\circ$. As with the results of Figure 11, the present method and the Euler predictions are essentially identical on the ogive nose for all three Mach numbers. On the cylindrical midbody, the comparison is also quite good at all Mach numbers for points ahead of the vicinity of the midbody/boattail juncture. Near that juncture, as well as on the boattail, some disagreement occurs. At $M_\infty = 0.75$, both methods indicate first a rapid positive then negative loading near the boattail

junction, with the loading remaining negative but gradually recovering toward zero along the boattail. At $M_\alpha = 0.90$, the present method essentially accentuates that behavior, while the Euler result indicates instead a rapid negative then positive loading near the boattail junction, and then an increasing negative loading along the boattail. This behavior of the Euler result is very similar to that in Figure 11, and reflects again a broad shock smearing due to grid coarseness.

Consequently, based on these and other related comparisons, we have concluded that the proposed transonically-corrected loading method is able to capture the primary nonlinear inviscid transonic effects which exist on typical ballistic projectiles.

STATIC AERODYNAMIC COEFFICIENTS FOR VARIOUS BOATTAIL PROJECTILES

The ultimate objective of the development of the TER solution procedure and the transonically modified loading method is in the prediction of the static aerodynamic coefficients of various boattail ballistic projectiles. In Figures 13-19 we provide results of the application of these procedures to a variety of different projectile shapes at conditions throughout the transonic regime.

Figure 13 exhibits a comparison of results from the present theory with 3-D TSD results and some limited data¹ for the variation of the overturning pitching moment coefficient C_{m_α} with oncoming Mach number M_α for an idealized M549 projectile having various conical boattail lengths. For both theoretical results, the actual nose was replaced by a sharp one of equal length, the rotating bands were neglected so that the cylindrical midbody was smooth, and the afterbody wake geometry was simulated by extending the conical boattail downstream. Three different boattail lengths on the basic projectile shape were considered, i.e., $l_{bt} = 0.579, 0.437, \text{ and } 0.242$, with the longest being that of the actual projectile. For the comparisons at $l_{bt} = 0.579$, indicated as solid lines, both theoretical methods display essentially identical variation with M_α and peak C_{m_α} value, but with the 3-D TSD results displaced forward in M_α by approximately 0.05. The range data indicate a slightly higher peak value, occurring at the same Mach number predicted by the present method.

The variation of the theoretical solutions for the two shorter boattails is noteworthy. Those results predict the occurrence of lower and earlier peaks in C_{m_α} with decreasing boattail length. This is consistent with both experimental findings and the fact that as the boattail length decreases the shock in that region will move off the boattail and into the wake at a lower Mach number. Additionally, there will exist a geometrically shorter moment arm for the negative loading created by the shock to act upon, thereby reducing the peak overturning moment. With regard to the comparisons between the two theoretical methods for the shorter boattail length, at $l_{bt} = 0.437$ the prediction of peak C_{m_α} is again quite close, with the present theory peak displaced rearward in M_α . At $l_{bt} = 0.242$, however, in addition to the rearward displacement of peak C_{m_α} values, the present method predicts a somewhat lower peak value as well. Without further details about the 3-D TSD results, it is difficult to identify precisely the cause of disagree-

ments. Clearly, however, both the variation trends and the general levels of the results are in quite reasonable agreement.

To examine the effect of various idealizations of projectile geometry that were made to facilitate some of these initial conditions, we have performed several parametric studies involving the independent variation of selected projectile geometry parameters. These have primarily involved investigating the idealizations of afterbody wake geometry and approximation of nose geometry, although a preliminary investigation of bore rider influence has also been made. Figure 14 provides the effect of different nose and afterbody wake geometry on the variation of C_{m_α} with M_∞ for the idealized M549 projectile, for which results for the sharp nose, and conical wake geometry model were presented previously in Figure 13. The four theoretical results include the following geometry combinations: (i) sharp nose, cylindrical wake, (ii) sharp nose, conical wake, (iii) blunt nose, conical wake, and (iv) blunt nose with fuze, conical wake. Limited range data¹ are also presented for the actual projectile. We note that the difference between the cylindrical and conical wake model results in the largest change in C_{m_α} ; with the continuous conical wake model most certainly being the more accurate simulation of the actual afterbody wake flow rather than the discontinuous cylindrical model. The shift in peak C_{m_α} location and the change to a more peaky behavior in the vicinity of the maximum resulting from the change from cylindrical to conical wake model confirms this, and exhibits excellent agreement with the range data. The addition of the blunt nose to the conical wake model projectile results in an upward shift in magnitude of C_{m_α} , but no essential difference in trend from the sharp nose result, and continues to bring the theoretical prediction in closer accord with the data near the maximum. The final addition of the fuze geometry to the blunt nose results in a similar but smaller change. The importance of modeling as much as possible of the geometric detail of the actual projectile, however, is clear.

In Figure 15, we present a similar comparison of theoretical results and range data for C_{m_α} versus M_∞ for a T388 projectile²⁰. That standard projectile has a 5.58 caliber overall length, 2.90 caliber ogive nose, and 0.59 caliber conical boattail with 7°37' boattail angle. Theoretical predictions are presented based on a (i) sharp nose, cylindrical wake, (ii) sharp nose, conical wake, and (iii) blunt nose, conical wake. As with the M549 projectile, the change from cylindrical to conical wake model brings the predicted results into almost exact agreement with the range data. Addition of the blunt nose in the theoretical calculation for this projectile results in a downward shift in C_{m_α} level, opposite to that of the M549, and indicating the interdependence of these geometric changes.

In Figure 16, we provide the final comparison between the present theory and range data for a standard conical boattail projectile. That figure compares theoretical results with both range and tunnel data²¹ for an improved 5"/54 projectile. This projectile is 5.20 calibers in length, with a 2.75 caliber ogive nose, and 1 caliber conical boattail with 7.5° boattail angle. The theoretical calculations exhibited are based on a conical afterbody wake model and blunt nose with fuze geometry included. Exhibited in the figure is the C_{m_α} versus M_∞ variation from $M_\infty = 0.5$ to 2.0, demonstrating the capability of the method throughout and beyond the transonic regime.

We note that the theoretical results agree very well for both overall trend and location of the peak pitching moment, with the magnitude and the predicted result being slightly higher throughout the entire range than the data indicate.

For this projectile, we performed several additional calculations to determine whether wind tunnel interference effects were present in the data. Accordingly, we determined the TER equivalent body outer flow solution subject to both a solid and various porous wall boundary conditions. These calculations were performed at Mach numbers at and in the vicinity of the $C_{m\alpha}$ peak. All of these calculations resulted in indiscernible changes from the free air result provided in Figure 16. We conclude that the discrepancy in $C_{m\alpha}$ level is most likely due to the midbody waisting on the actual projectile²¹, which was not modeled in the theoretical calculations.

In the next three figures, Figures 17-19, we present results which demonstrate the capability of the present predictive method to treat a variety of different projectile boattail shapes, both axisymmetric and non-axisymmetric. Figure 17 presents the predicted variation of $C_{m\alpha}$ with M_∞ for the four different boattail shape projectiles shown previously in Figures 1 and 6, plus an additional conical boattail projectile with shorter boattail ($l_b = 0.5$) length. All of these projectiles have a 5 caliber overall length and identical 2 caliber sharp ogive nose geometry. Consequently, the results presented illustrate, in a design sense, the effect on $C_{m\alpha}$ of varying the boattail shape through a wide range of geometries. We note that the 1 caliber conical boattail projectile exhibits the highest $C_{m\alpha}$ and thus is the worst choice from a stability design criterion. Decreasing the conical boattail length to 0.5 calibers improves the situation somewhat, but not significantly. The square boattail further improves the situation, but the triangular boattail, of these four shapes, provides the best result for minimum peak $C_{m\alpha}$. These results are in direct correspondence with the experimental results of Reference 2. Although the cylindrical boattail exhibits the lowest peak C_m , its high drag and consequent low range make it an undesirable candidate shape.

In Figure 18, we present the corresponding results for the normal force coefficient C_N for these same five shapes. We note the prediction that the longer conical boattail has the lowest lift of all the projectiles, due to the strong negative loading on the boattail section.

In Figure 19, we exhibit the surface pressure drag coefficient variation with M_∞ for these same projectiles. This calculated drag represents the wave drag of these various shapes. In order to determine the total inviscid drag, those results must be augmented by the base pressure drag. This could be done within the framework of the present computational procedure either from a correlation of base pressure drag and inviscid base pressure, or through a boundary layer/wake computation coupled to the inviscid flow prediction. The point of presenting these results is to indicate the means for a first-order approximation of the projectile drag is feasible with the present theoretical procedure.

Finally, we note the computational efficiency of the present method. A complete calculation (TER calculation plus loading determination) requires less than 30 seconds CPU time on a CDC 7600 for a typical projectile at a

specified M_∞ . As a typical example, regard to the theoretical predictions of C_{m_0} , C_{N_0} , and C_D provided in Figures 17 through 19 involving the 5 different boattail projectiles. The separate points on each of the curves indicate the individual calculations made and total 110 separate TER and loading solutions. Computational time for all of these cases was less than 30 minutes of CDC 7600 CPU time.

POTENTIAL APPLICATION TO MISSILES AT HIGH ANGLE OF ATTACK

In this section, we point out the potential utility of the concepts and procedures developed here to applications involving current missile configurations and requirements. In the current applications of the TER procedure to ballistic projectiles, attention was focused on the low to moderate lift situation (thickness-dominated flows). This was done because that lift range is the necessary operating regime for these shapes, since current ballistic projectiles are spin stabilized and have no means (no lifting surfaces) of recovering from a high angle of attack condition. For applications to present-design missiles, however, which often employ both canard and tail surfaces, the control situation is quite different and the operation requirements imposed usually require capability of operating at high angle of attack. Under such conditions, the primary nonlinear effects²² arise from compressibility effects and the various vortical flows (nose, canard, afterbody, and tail vortex systems) generated by different segments of the missile surface. At transonic conditions, both of these nonlinear effects can be treated by employing the lift-dominated limiting form the TER. Figure 20 provides an illustration of the application of the TER to such configurations at high angle of attack transonic conditions; together with the decomposition of the flow into its various inner and outer components. In that illustration, for clarity of presentation, we have omitted indicating the nose and afterbody vortices, and have only shown the canard trailing vortices. In the actual TER application and calculation, all of these vortical flows would be accounted for.

As shown in Figure 20, the various component problems in the inner region now consist of both vertical and horizontal translation of the cross section corresponding to upwash and sidewash, the crossflow vortical flow field consisting of all vortices generated upstream of a particular longitudinal station, and the familiar thickness problem, whereas the outer flow now consists of axial flow past both an equivalent source and doublet distribution in which the source distribution consists of the equivalent area source distribution augmented by additional source-like terms due to the axial and spanwise lift distribution⁵.

Although the outer problem is now three-dimensional, the TER provides a means for solution that is nevertheless significantly simpler than solving the full nonlinear three-dimensional flow problem past the actual configuration. In light of the success of the TER method for ballistic projectile applications, it is felt that the potential of the method for providing an accurate and computationally-efficient solution to the transonic high angle of attack slender missile problem is high.

CONCLUDING REMARKS

The development of a theoretical predictive method for determining the steady inviscid aerodynamic behavior of ballistic projectiles throughout the

transonic regime is described. The emphasis of the work was directed toward establishing the capability for investigating the now standard conical boattail projectiles as well as a variety of new shapes characteristic of the non-axisymmetric boattail projectiles under current study by the U.S. Army. The final objective is the development of a rational modeling procedure for the investigation of the transonic aerodynamic effects of incorporating different boattail and body geometries into ballistic projectile design, with a view toward optimizing the aerodynamic performance of these shapes, such as increasing range and/or payload while simultaneously avoiding stability problems.

The theoretical analysis is based on the transonic equivalence rule (TER) and includes a finite-difference SLOR procedure for determining the nonlinear axisymmetric outer (far field) flow about the "equivalent" body of revolution, and a two-dimensional finite-element solver for providing general solutions to the inner (near field) cross-flow problem for the arbitrary geometries characteristic of the new boattail projectiles. The ultimate utility of the predictive method is in the accurate determination of the static aerodynamic characteristics of these projectiles, specifically the lift and destabilizing pitching moment. Toward that end, a new nonlinear loading calculation procedure which incorporates transonic effects has been formulated and tested. The technique is based on apparent mass concepts and employs the finite-element inner crossflow solver to determine the appropriate apparent mass coefficients and uses the nonlinear outer TER solution for the axisymmetric flow about the equivalent body to account for nonlinear effects due to shock waves.

Results are presented for a wide variety of projectile shapes, having both axisymmetric and nonaxisymmetric boattail geometries, and demonstrates the ability of the procedure to predict successfully the observed range and tunnel variations of pitching moment and normal force throughout the transonic range. Additional calculations illustrating the separate effects of different geometry models to simulate the afterbody wake and nose bluntness including fuze geometries are presented.

ACKNOWLEDGEMENT

This research was supported by the U.S. Army Research Office under Contract DAAG29-77-C-0038 with Dr. Robert Singleton as Technical Monitor.

REFERENCES

1. Reklis, R. P., Sturek, W. V., and Bailey, F. R.: Computation of Transonic Flow Past Projectiles at Angle of Attack. AIAA Paper No. 78-1182, July 1978.
2. Platou, A. S.: Improved Projectile Boattail. AIAA Jour., Vol. 12, Dec. 1975, pp. 727-732.
3. Heaslet, M. A. and Spreiter, J. R.: Three-Dimensional Transonic Flow Theory Applied to Slender Wings and Bodies. NACA Rept. 1318, 1957.
4. Cheng, H. K. and Hafez, M. M.: Equivalence Rule and Transonic Flows Involving Lift. Dept. of Aero. Eng. Rept. USCAE 124, Univ. of Southern

California, School of Engineering, Apr. 1973.

5. Cheng, H. K. and Hafez, M. M.: Transonic Equivalence Rule: A Nonlinear Problem Involving Lift. J. of Fluid Mech., Vol. 72, 1975, pp. 161-188.
6. Oswatitsch, K.: Die Theoretischen Arbeiten über schallnahe Strömungen am Flugtechnischen Institut der Kungl. Techniska Högskolan, Stockholm. Eighth Inter'l Congress on Theoretical and Applied Mechanics, Istanbul, 1952, (1953) pp. 261-262.
7. Oswatitsch, K.: The Area Rule. Applied Mech. Reviews, Vol. 10, Dec. 1957, pp. 543-545.
8. Spreiter, J. R.: Theoretical and Experimental Analysis of Transonic Flow Fields. NACA-Univ. Conf. on Aerodynamics, Construction, and Propulsion II, "Aerodynamics," 1954, pp. 18-1 - 18-17.
9. Barnwell, R. W.: Transonic Flow About Lifting Configurations. AIAA Jour., Vol. 11, May 1973, pp. 764-766.
10. Bailey, F. R.: The Numerical Calculation of Transonic Flow about Slender Bodies of Revolution. NASA TND-6582, Dec. 1971.
11. Krupp, J. A. and Murman, E. M.: Computation of Transonic Flows Past Lifting Airfoils and Slender Bodies. AIAA Jour., Vol. 10, July 1972, pp. 880-886.
12. Murman, E. M.: Analysis of Embedded Shock Waves Calculated by Relaxation Methods. AIAA Jour., Vol. 12, May 1974, pp. 626-633.
13. Jameson, A.: Transonic Flow Calculations. VKI Lecture Series 87, Computational Fluid Dynamics, von Kármán Institute for Fluid Dynamics, Rhode-St. Genesee, Belgium, Mar. 1976.
14. Stahara, S. S. and Spreiter, J. R.: Transonic Wind Tunnel Interference Assessment-Axisymmetric Flows. AIAA Jour., Vol. 18, Jan. 1980, pp. 63-71.
15. Bryson, A. E., Jr.: Stability Derivatives for a Slender Missile with Application to a Wing-Body-Vertical Tail Configuration. J. Aeronaut. Sci., Vol. 20, No. 5, 1953, pp. 297-308.
16. Nielsen, J. N.: Missile Aerodynamics. McGraw-Hill, New York, 1960.
17. Stahara, S. S. and Spreiter, J. R.: Transonic Flows Past Nonaxisymmetric Slender Shapes - Classical Equivalence Rule Analysis. AIAA Jour., Vol. 17, No. 5, Mar. 1979, pp. 245-252.
18. Reklis, R. P., Danberg, J. F., and Ingu, G. R.: Boundary Layer Flows on Transonic Projectiles. AIAA Paper No. 79-1551, July 1979.
19. Klopfer, G. H. and Chaussee, D. S.: Numerical Solution of Three Dimensional Transonic Flows Around Axisymmetric Bodies at Angle of Attack. Nielsen Engineering & Research, Inc. TR 176, Feb. 1979.

20. Krial, K. S. and MacAllister, L. C.: Aerodynamic Properties of a Family of Shell of Similar Shape--105mm XM308E5, XM308E6, T388 and 155mm T387. BRL Memo Rept. No. 2023, Feb. 1970.
21. Ohlmeyer, E. J.: Dynamic Stability of the Improved 5"/54 Projectile. NWL Tech. Rept. TR-2871, Dec. 1972.
22. Nielsen, J. N.: Wright Brothers Lectureship in Aeronautics, Missile Aerodynamics - Past, Present, and Future. AIAA Paper No. 79-1819, Aug. 1979.

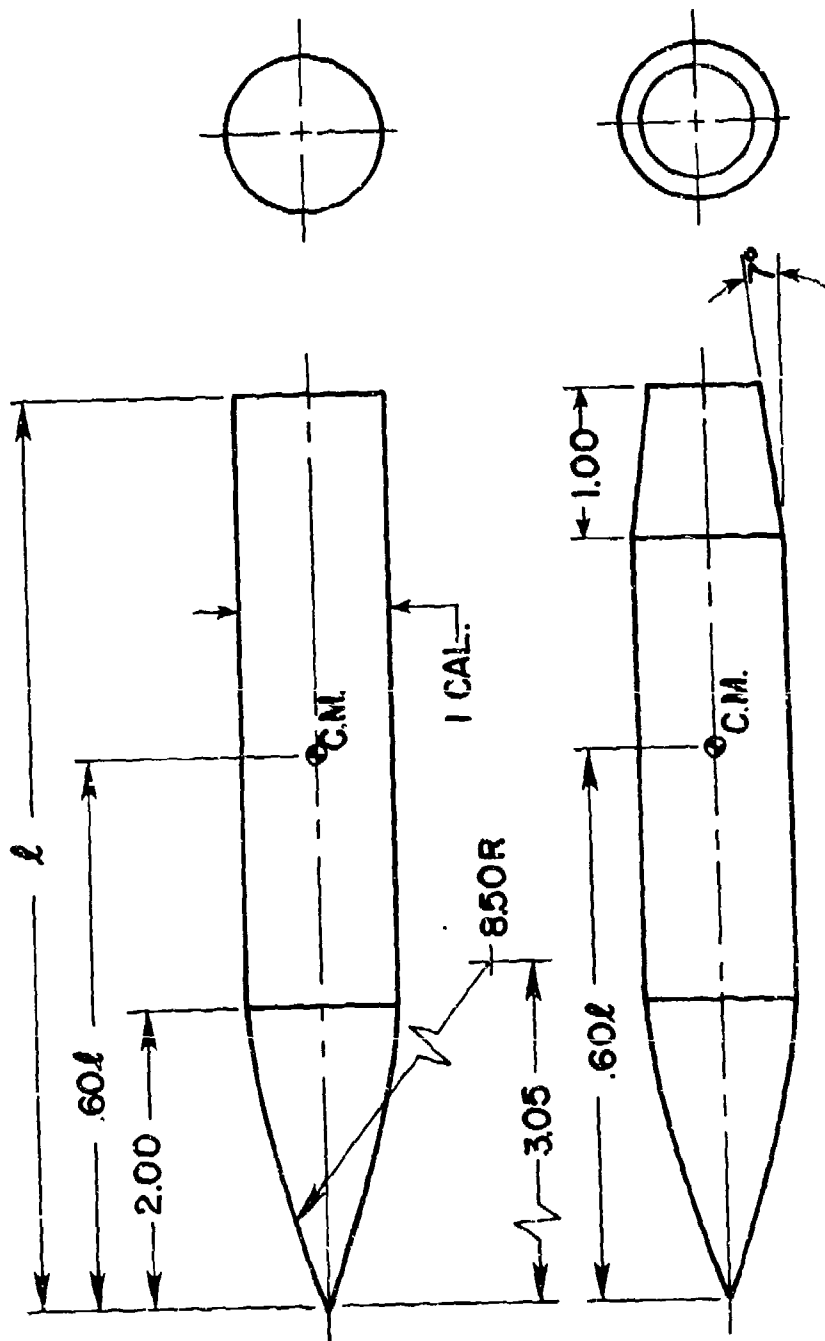
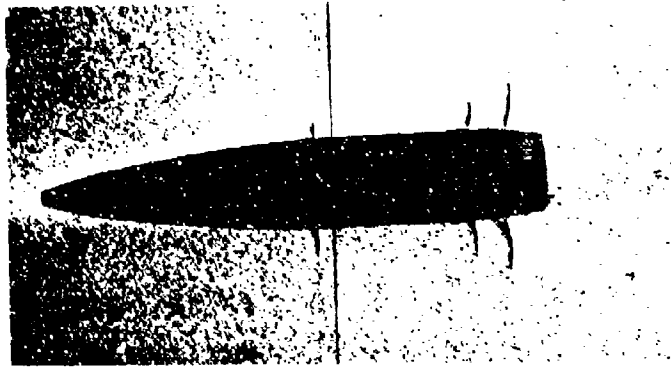
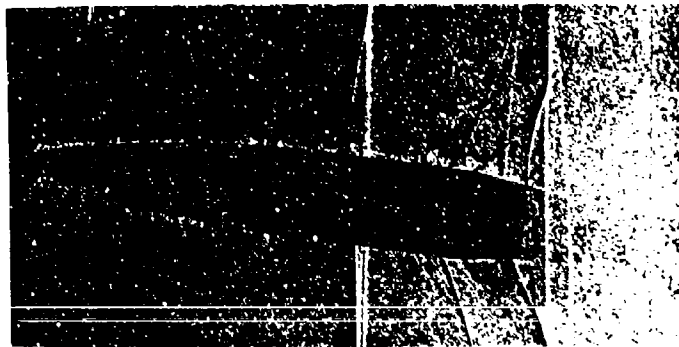


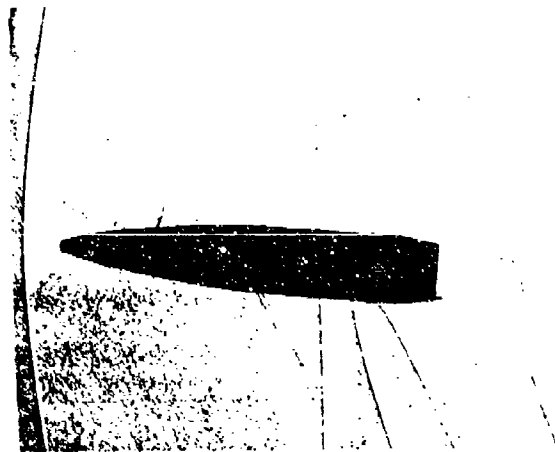
Figure 1 Illustration of typical ballistic projectiles having cylindrical and conical boattails; dimensions in calibers.



a. $M_{\infty} = 0.898$



b. $M_{\infty} = 0.957$



c. $M_{\infty} = 1.033$

Figure 2 Shadowgraphs of ballistic projectiles at various transonic Mach numbers illustrating characteristic shock formation and movement.

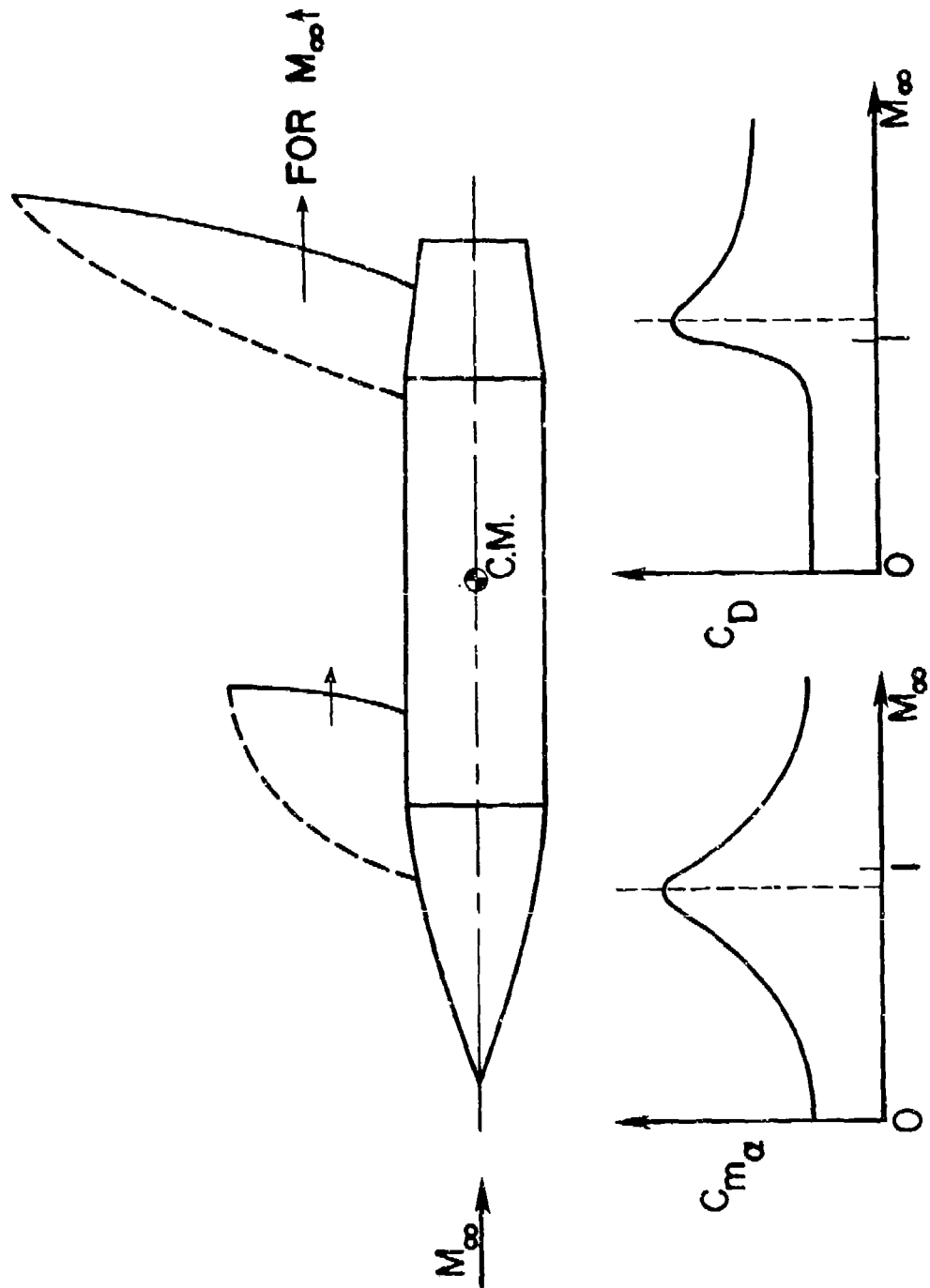


Figure 3 Variation of shock movement, destabilizing pitching moment, and drag with M_∞ on a typical ballistic projectile.

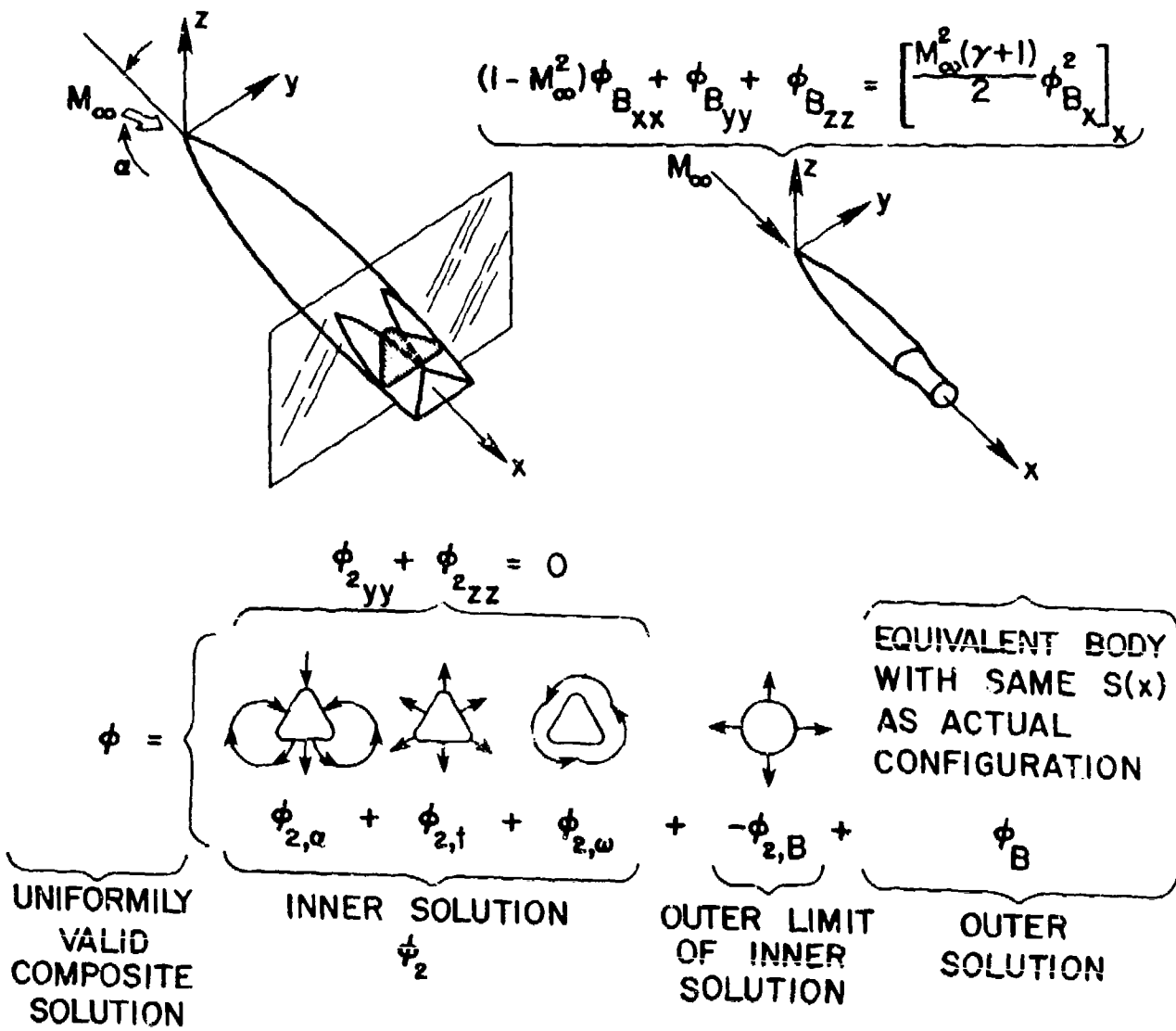
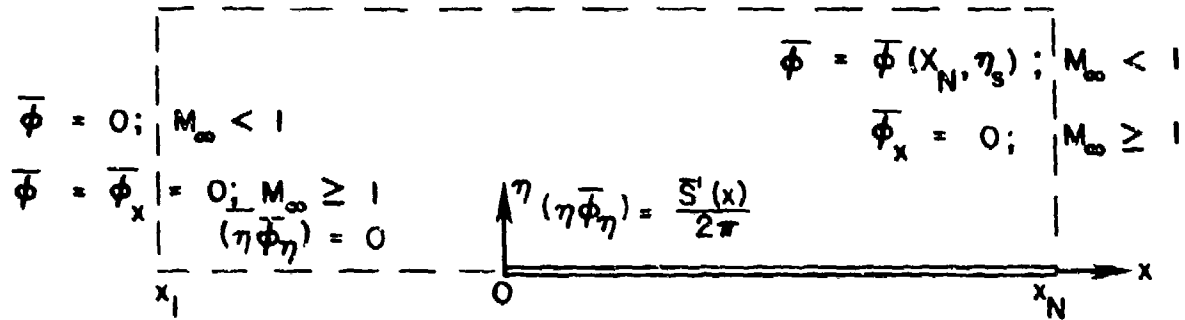


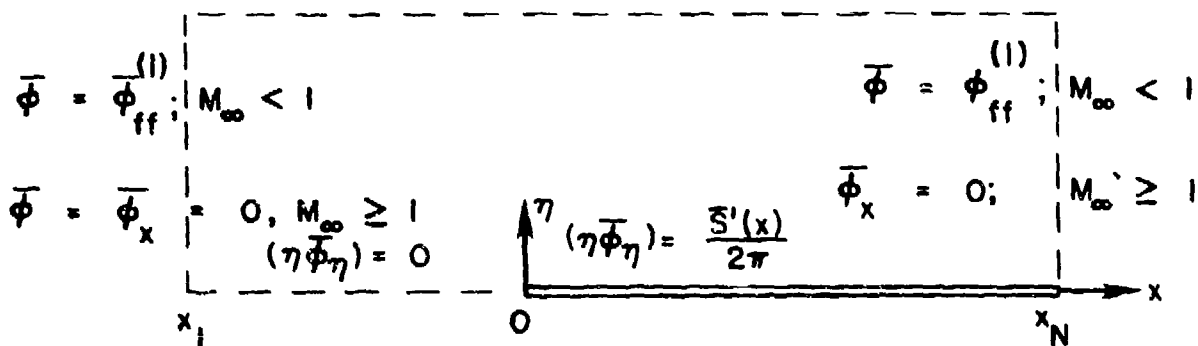
Figure 4 Illustration of the classical transonic equivalence rule for slender configurations

$$\bar{\phi} = \frac{1}{P} \int_{x_1}^x \bar{\phi}_\eta (\xi, \eta_s) d\xi$$



WIND TUNNEL

$$\bar{\phi} = \phi_{ff}^{(1)}$$



FREE AIR

Figure 5 Summary of boundary conditions for outer flow computational problem.

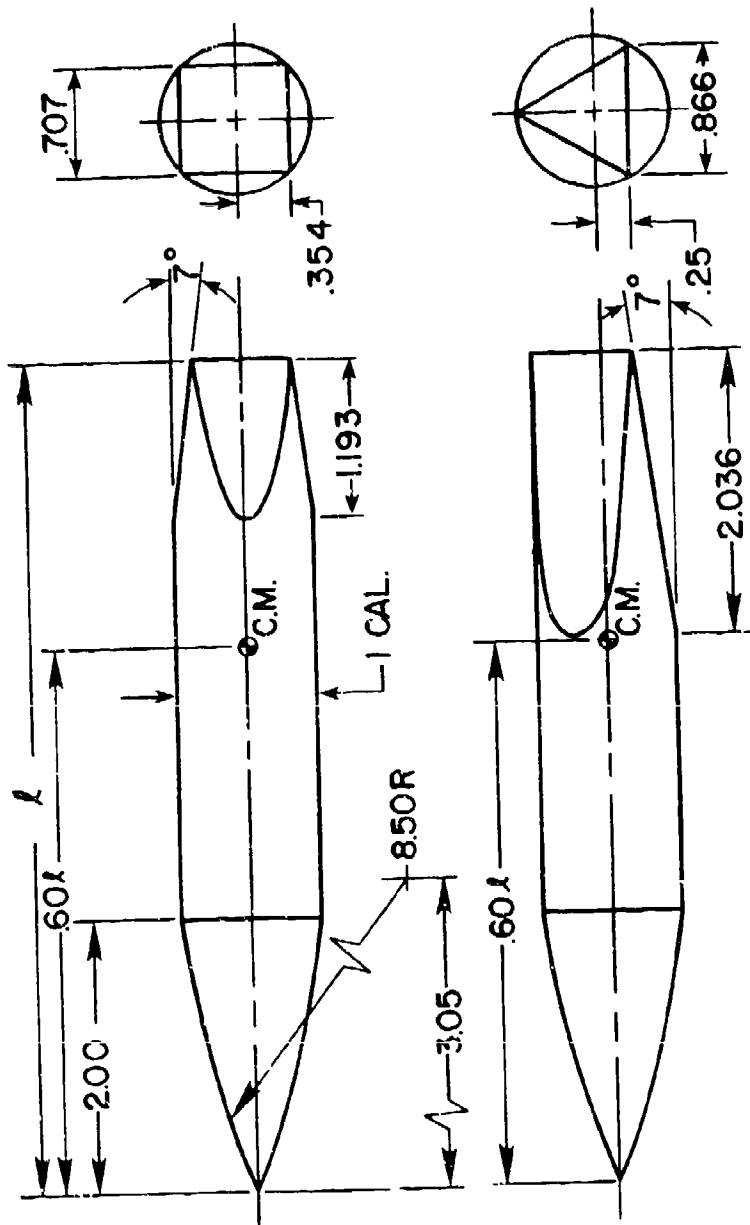
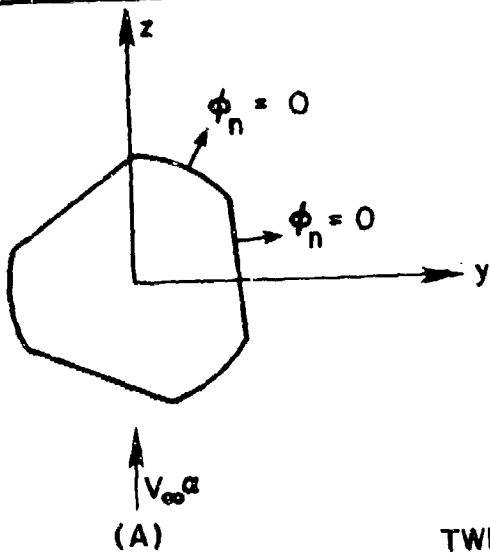
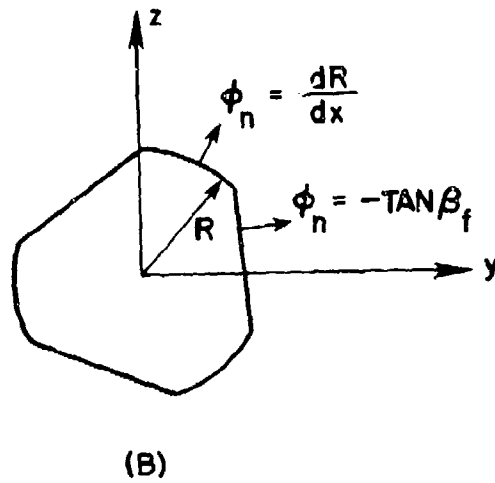


Figure 6 Ballistic projectiles having inscribed square and triangular boattail shapes formed by cutting planes acting on the cylindrical boattail section.

CROSSFLOW: $\phi_{2,\alpha}$



CONTRACTION: $\phi_{2,t}$



TWIST: $\phi_{2,\omega}$

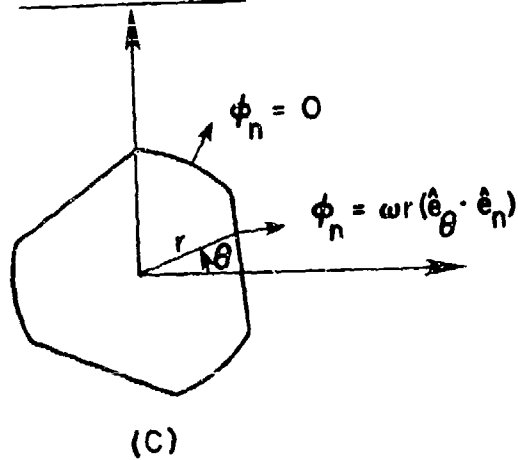


Figure 7 Body surface boundary conditions for inner flow computational problem.

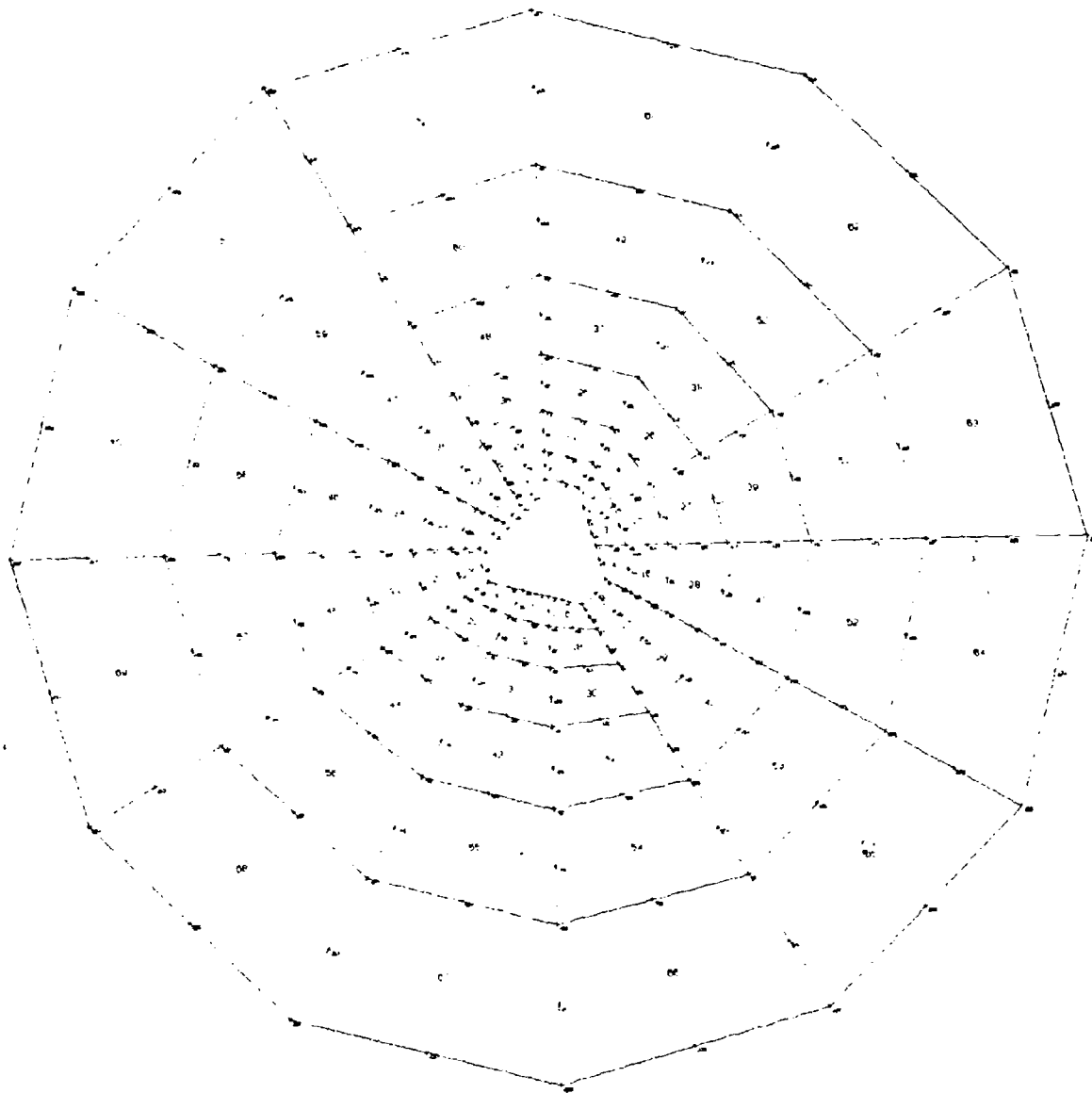


Figure 8 Illustration of typical finite-element mesh employed for inner problem.

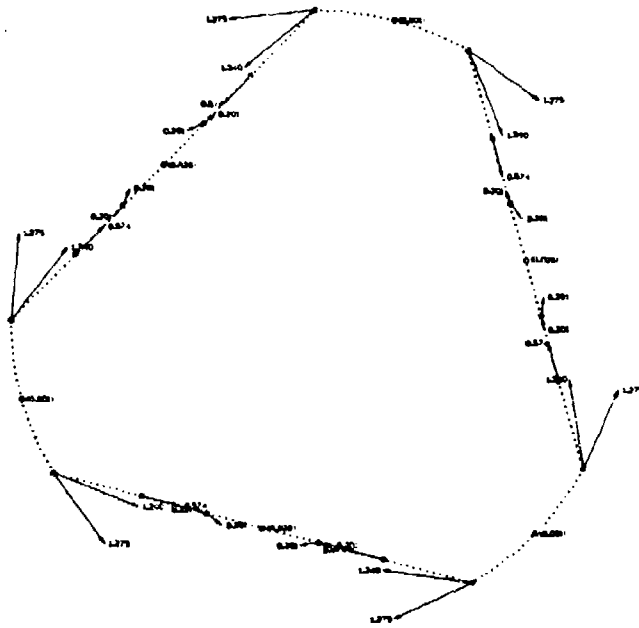


Figure 9 Body surface crossflow velocities predicted by finite-element solver for a typical contraction inner problem, viewed relative to local surface.

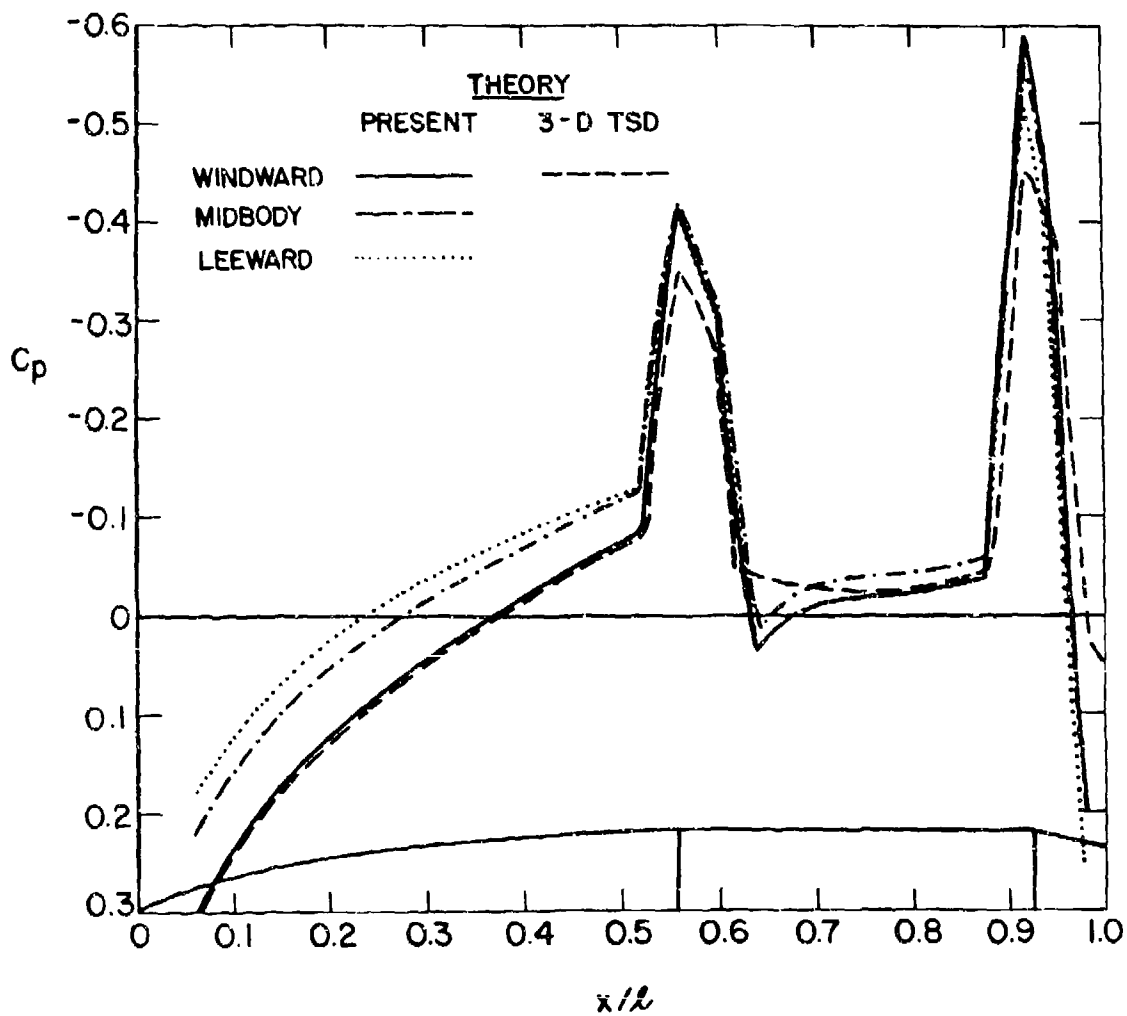


Figure 10 Prediction of surface pressures on a secant ogive/cylinder/7° conical boattail projectile at $M_\infty = 0.94$, $\alpha = 4^\circ$.

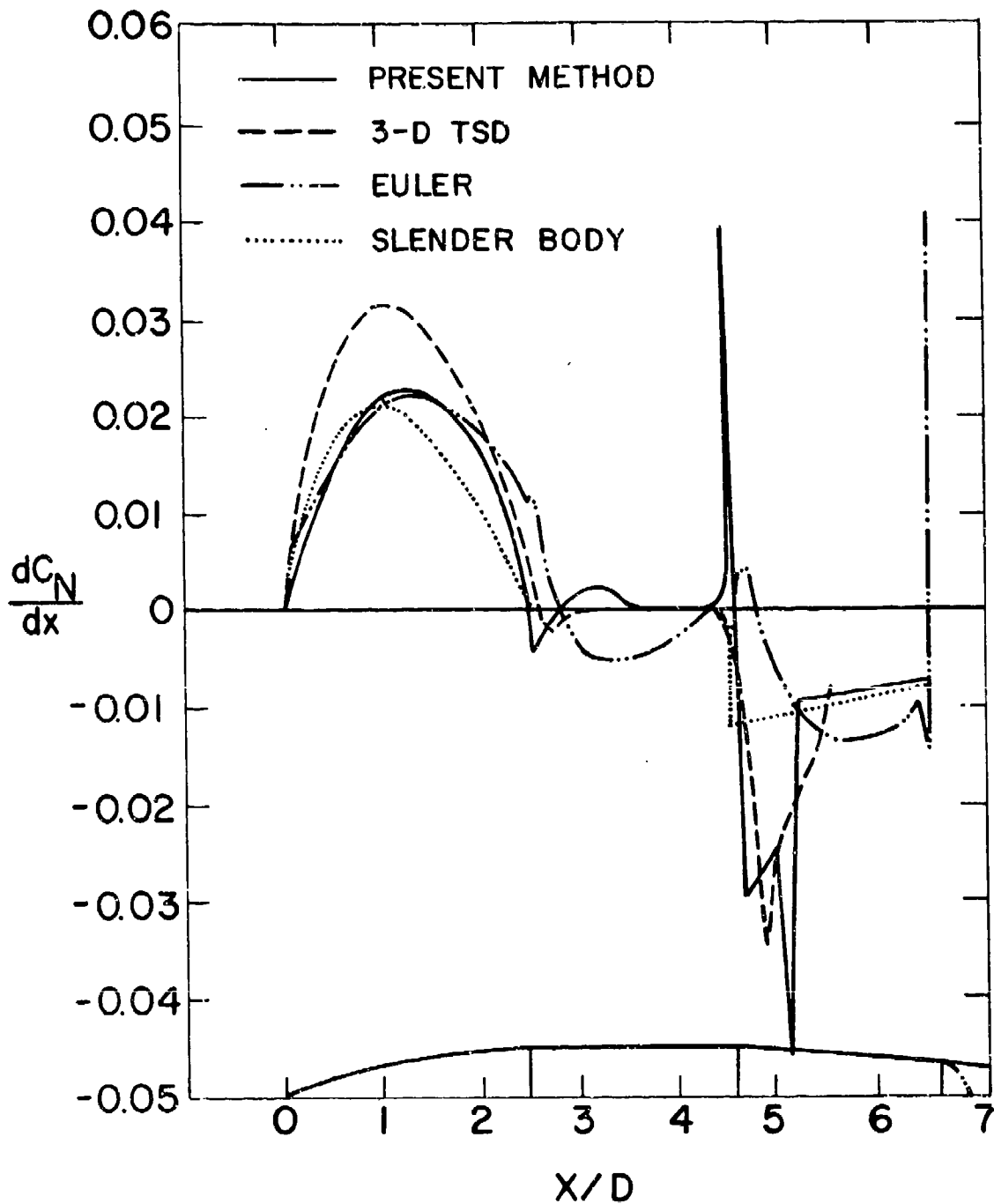


Figure 11 Comparison of present loading method with other theoretical methods for the normal force loading distribution on an idealized M549 projectile at $M_\infty = 0.95$, $\alpha = 1^\circ$.

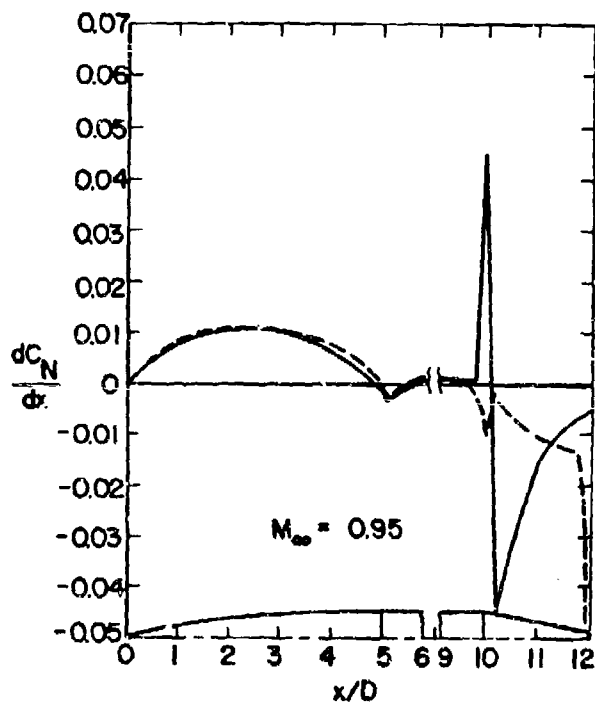
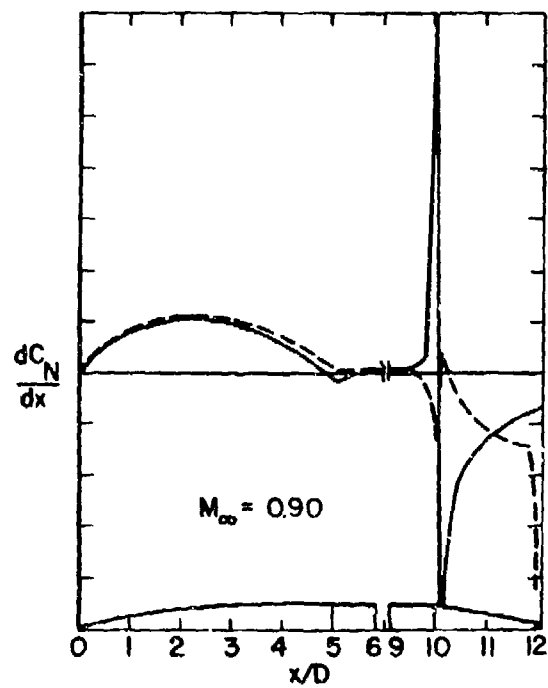
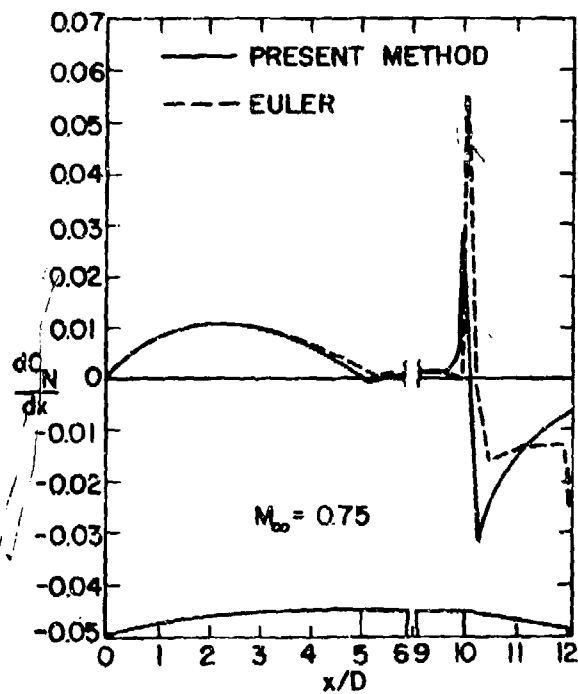


Figure 12 Comparison of present loading method with 3-D Euler equation results for the normal force loading distribution on a slender 12 caliber length projectile at various transonic Mach numbers.

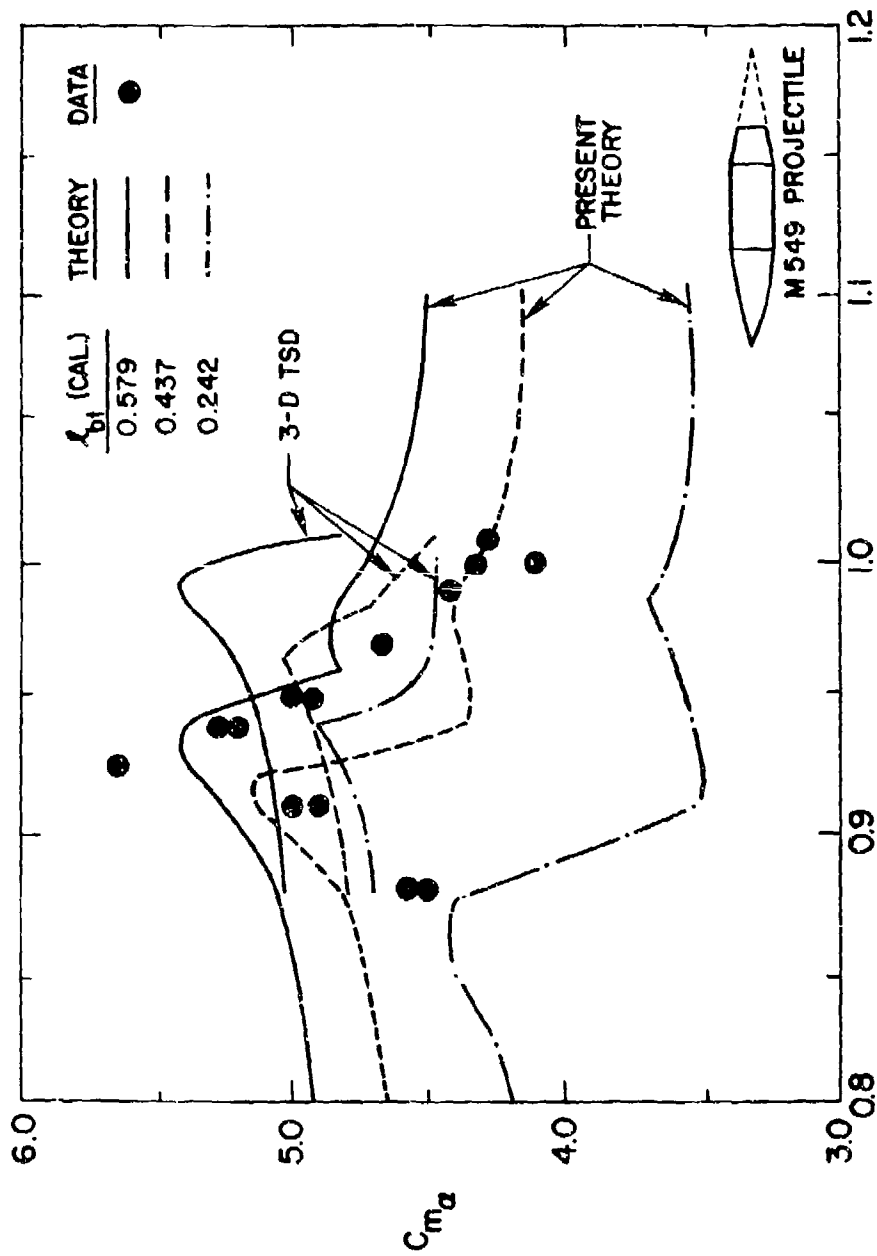


Figure 13 Comparison of present method with 3-D TSD results and data for the variation of destabilizing pitching moment C_{m_α} with M_∞ for a basic M549 projectile having various boattail lengths.

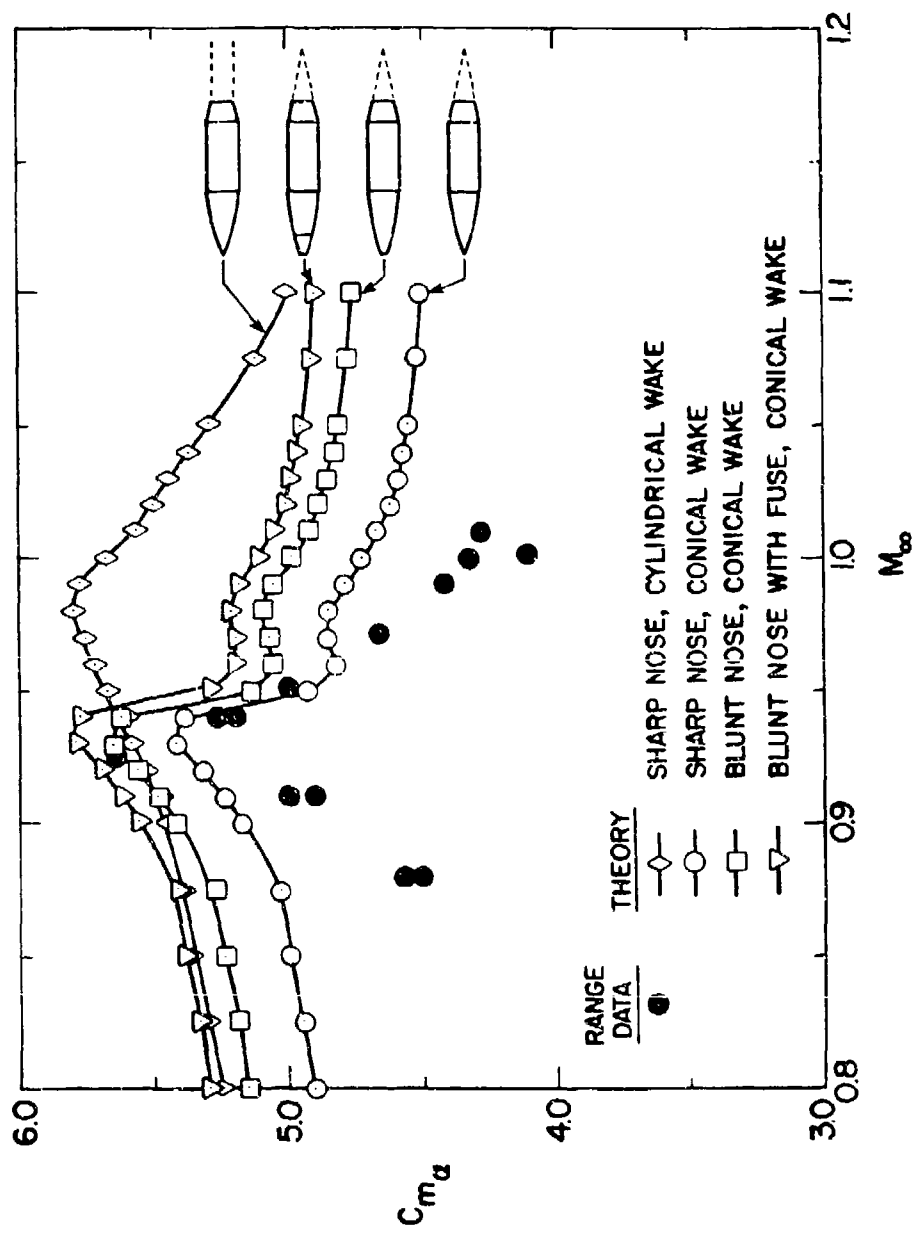


Figure 14 Effect of afterbody wake geometry and nose bluntness on variation of $C_{m\alpha}$ with M_∞ for a M549 projectile.

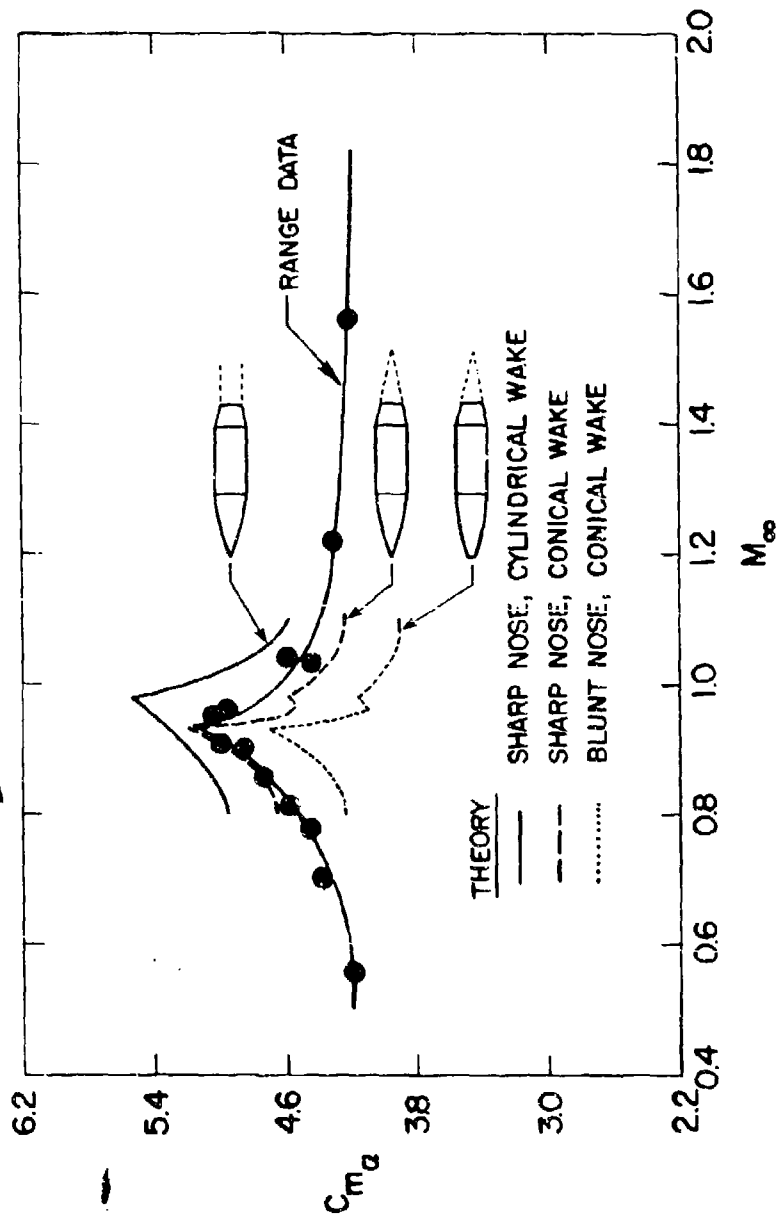


Figure 15 Comparison of theoretical results and data for the variation of C_m versus M_∞ for a T388 projectile illustrating the effect of wake geometry and nose bluntness

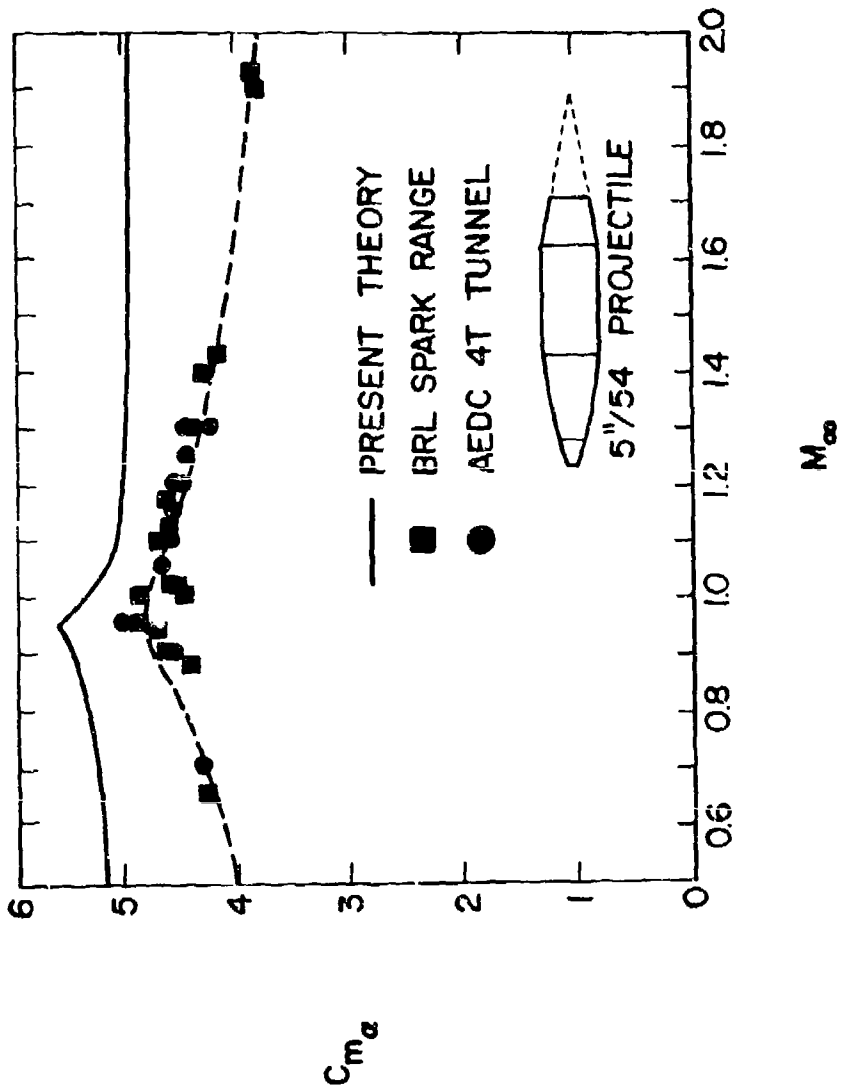


Figure 16 Comparison of theoretical results and data for the variation of $C_{m\alpha}$ versus M_∞ for the improved 5"/54 projectile.

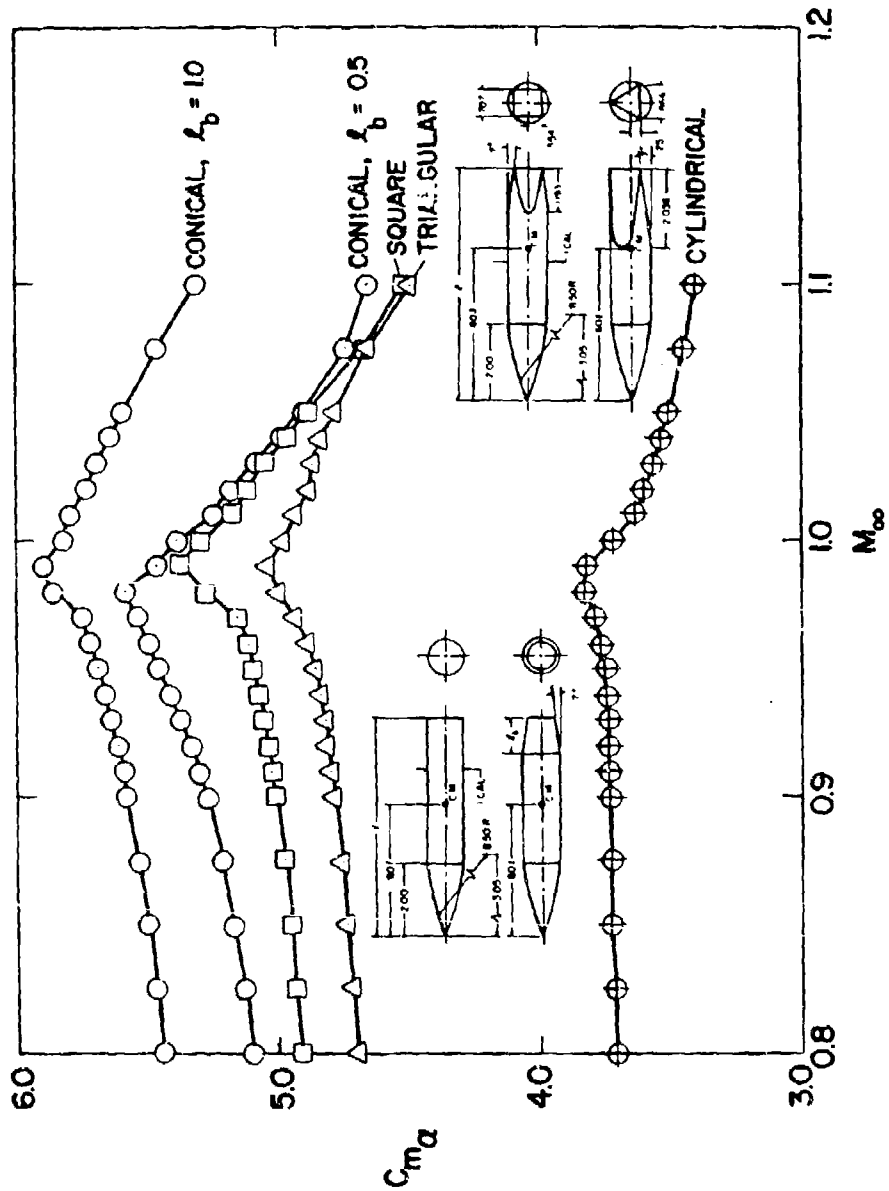


Figure 17 Effect of various boattail geometries on $C_{m\alpha}$ variation with M_∞ for a 5 caliber length, fixed nose geometry projectile.

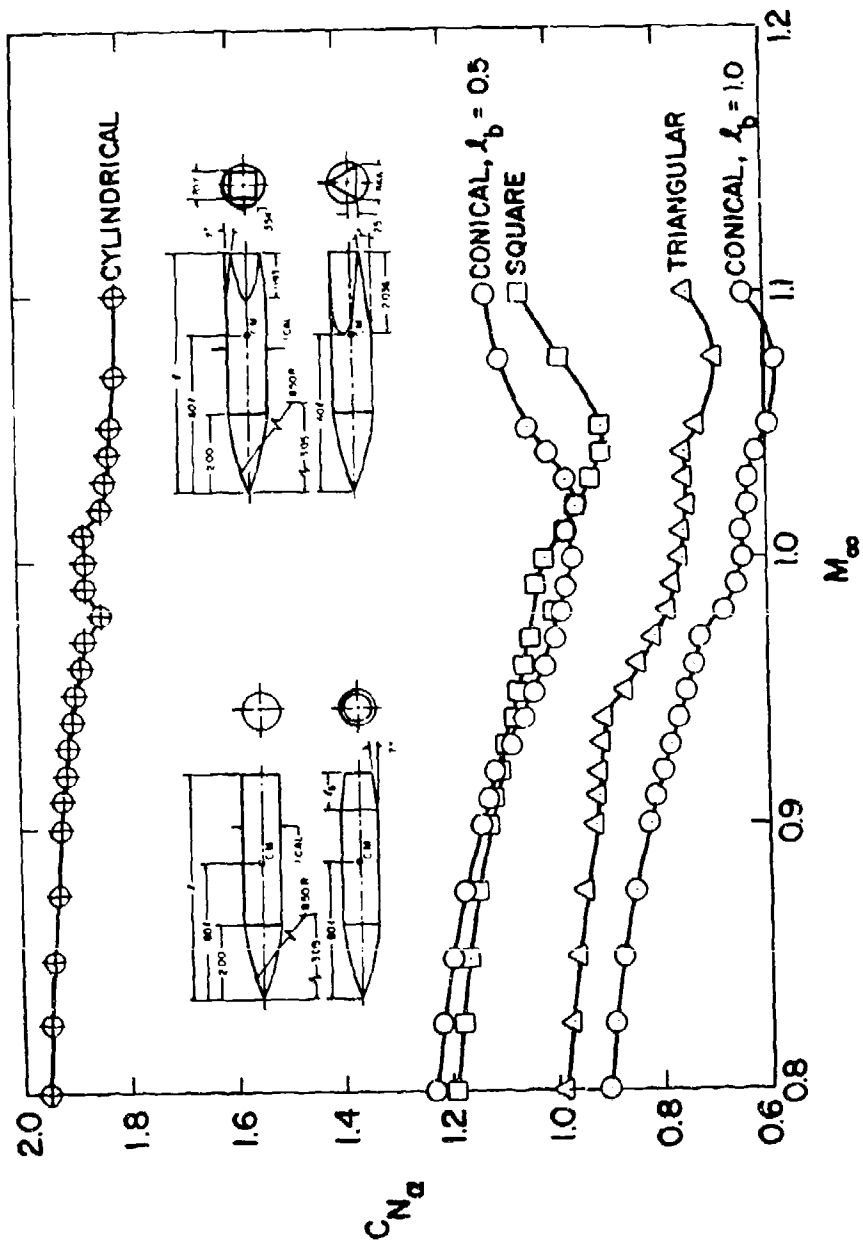


Figure 18 Effect of various boattail geometries on $C_{N\alpha}$ variation with M_∞ for a 5 caliber length, fixed nose geometry projectile.

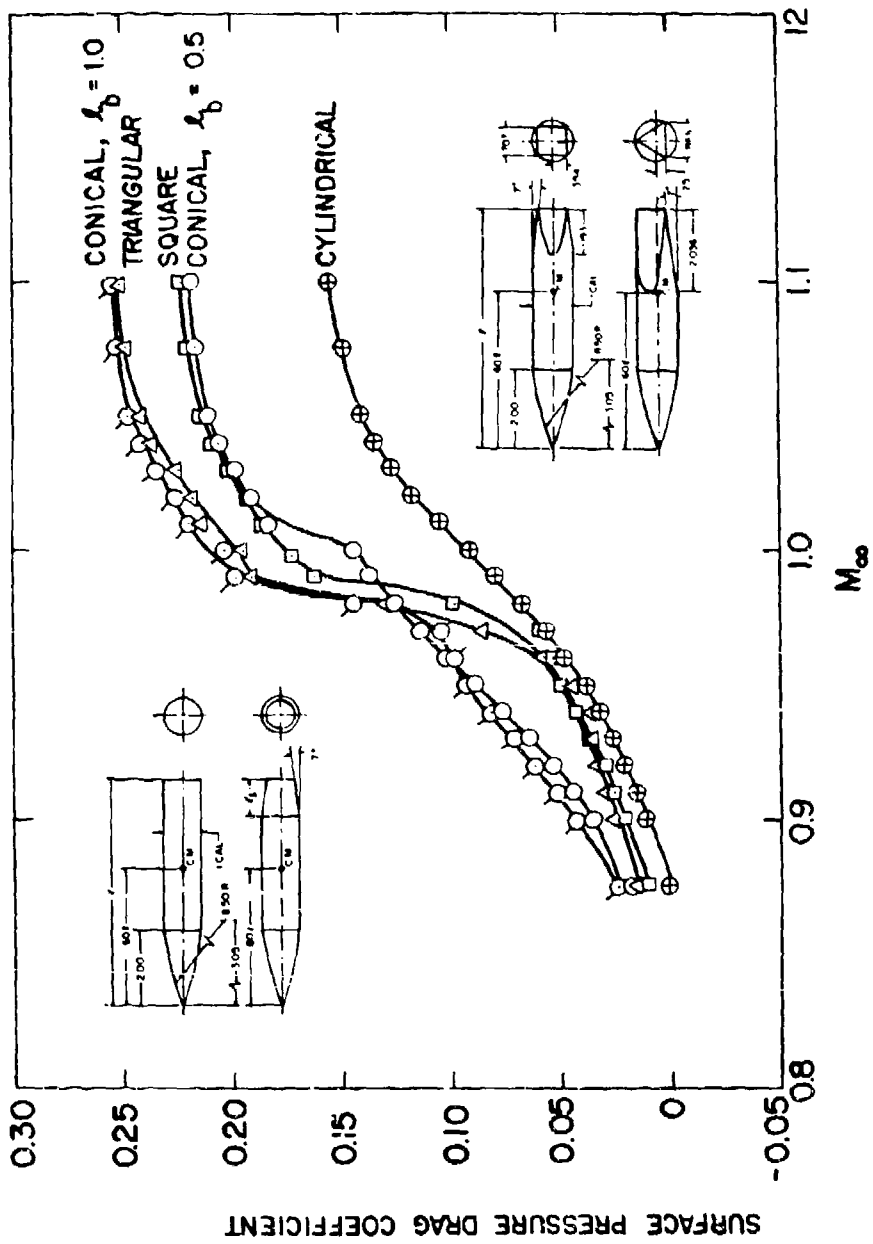


Figure 19 Effect of various boattail geometries on C_D variation with M_∞ for a 5 caliber length, fixed nose geometry projectiles.

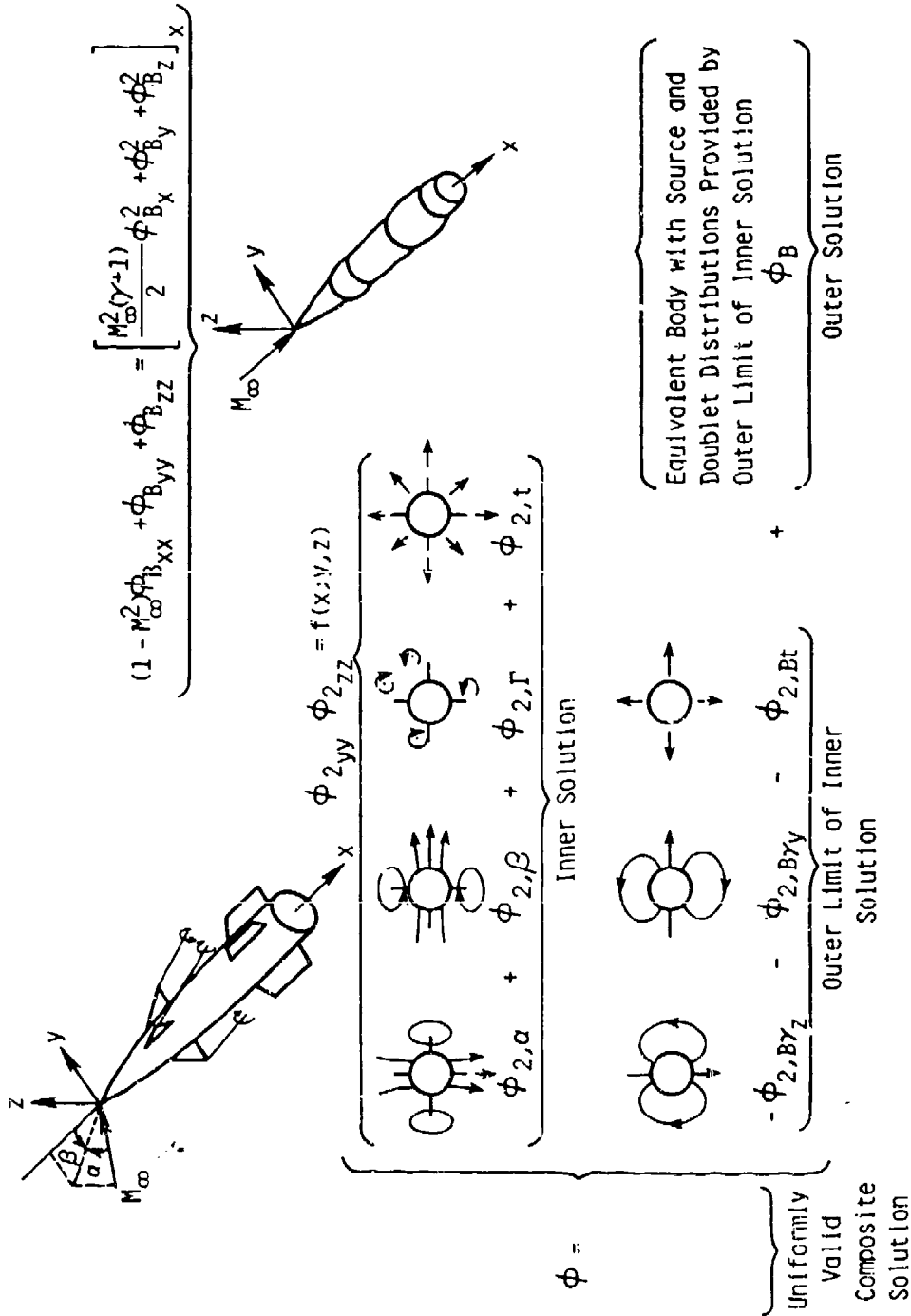


Figure 20 Application of transonic equivalence rule concepts to typical canard-cruiform tail missile configurations at high angle of attack transonic conditions.